




Cite this: DOI: 10.1039/d2tc02127g

Progress in ultraviolet photodetectors based on II–VI group compound semiconductors

Jiang Wang, Yue Xing, Fang Wan, Can Fu, Chen-Hao Xu, Feng-Xia Liang and Lin-Bao Luo *

Ultraviolet (UV) photodetectors (PDs) have found widespread application in various fields, such as environmental protection, life sciences, secure communications, automated systems, and missile tracking, which renders UVPDs the most important component in modern optoelectronic devices and systems. In the past decade, a large number of UVPDs with various device structures and fast response speed have been reported. While most of the UVPD devices are usually assembled from Si and other semiconductor materials, II–VI group semiconductors (ZnS, ZnSe, etc.), which have a wide bandgap and high exciton binding energy, are regarded as potentially important candidates for high-performance UVPD application as well. In this review, we comprehensively discuss the basic concepts and operation mechanisms of UVPDs, which are key factors for rational comparison between different photodetectors. In addition, the main research status of UVPDs based on II–VI group semiconductors is reviewed. Some emerging techniques to optimize device performance are discussed as well. Due to the trade-off between the two key parameters of the responsivity and response time, the ultimate performance of some II–VI group semiconductor-based UVPDs remains inadequate. And then, the initial applications based on II–VI group semiconductor photodetectors are mentioned. Finally, the current challenges and future directions of II–VI group semiconductor-based UVPDs are outlined and discussed, and general advice for realizing novel high-performance photodetectors and their applications is given to provide a guideline for the future development of this fast-developing field.

Received 23rd May 2022,
Accepted 7th August 2022

DOI: 10.1039/d2tc02127g

rsc.li/materials-c

1. Introduction

UV radiation plays a vital role in the human environment and affects the survival and development of almost all living organisms. The German physicist Johann Wilhelm Ritter first discovered UV radiation in 1801. In subsequent studies, researchers identified multiple wavelengths of UV radiation and divided the UV spectrum into three bands: UV-A (320–400 nm), UV-B (280–320 nm), and UV-C (100–280 nm).^{1–3} Further research shows that UV radiation has great application potential in the fields of sterilization and disinfection, electronics, biomedicine, air purification, etc. However, high levels of UV radiation may lead to a significant increase in the incidence rate of skin cancer in humans. Thus, the study of UV photo-detection has attracted much attention from scientists. Based on Einstein's photoelectric effect, UVPDs for transforming UV radiation signals into electronic signals have been developed by scientists. A high-performance UVPD has "5S" requirements (high sensitivity, high signal-to-noise ratio, high speed, high spectral selectivity, and high stability).⁴ From the perspective of

energy band theory, semiconductors with a bandgap larger than 3.0 eV (e.g. GaN, SiC, and AlGaN) are ideal materials for the fabrication of UVPD devices.^{1,2,4,5} For this reason, the past decade has witnessed great progress in the development of various sensitive UVPDs with different device geometries, and many review papers have been published regarding wide bandgap semiconductor based UVPDs. As an alternative, Si UVPDs are also an important candidate for UV detection in the market because of their good compatibility with the existing semiconductor manufacturing technology. However, it is undeniable that, due to the relatively small bandgap of Si (1.1 eV), Si-based photodetectors generally require a complex filter structure that increases the fabrication cost and volume of the device.^{5,6}

II–VI Group semiconductors (ZnS, CdS, ZnSe, etc.) have been widely used for the fabrication of UVPDs in recent years due to their large bandgap, high exciton binding energy and exciton gain, good optical properties, and excellent thermal and environmental stabilities.^{7–10} In addition, II–VI group semiconductors have higher electron and hole mobilities than those of other semiconductor materials with a similar bandgap.¹¹ Another important property is the direct band structure of II–VI group semiconductors, which determines the interband radiative recombination of electrons and holes, and the high efficiency of electron–hole pair

School of Microelectronics, Hefei University of Technology, Hefei, Anhui, 230009, China. E-mail: luolb@hfut.edu.cn

Table 1 Summary of the representative parameters of II–VI group semiconductors

Materials	Crystal structure	Bandgap (eV)	Electron mobility ($\text{cm}^2 \text{V}^{-1} \text{s}^{-1}$)	Dielectric constant	Effective electron mass	Ref.
ZnS	Wurtzite	3.7	285	8.3	$0.34 m_0$	28–30
CdS	Cubic	2.42	350	8.9	$(0.18 \pm 0.05) m_0$	29, 31 and 32
ZnSe	Cubic	2.7	502	10.2	$0.17 m_0$	33 and 34
ZnSSe	Hexagonal	2.7–3.7	126	5.8–6.1	$\sim 0.15 m_0$	35–38
ZnCdS	Cubic/hexagonal	2.4–3.5	—	~ 3.1	$0.37 m_0$	38–42

generation after the absorption of photons. On the other hand, compared with many II–VI group semiconductors, ZnO, as a typical II–VI group oxide semiconductor, has been widely used in various optoelectronic devices such as lasers, LEDs, and UVPDs. In recent years, plenty of excellent review papers have summarized the progress of ZnO-based UVPDs.^{12–16} However, there are few reviews on other II–VI group semiconductor (ZnS, CdS, ZnSe, *etc.*) UVPDs.

Table 1 lists some basic parameters of II–VI group semiconductor materials mainly used in UVPDs. Among them, the bandgap of the ternary alloys ZnSSe and ZnCdS can be regulated by adjusting the element contents. Currently, many high-performance photodetectors based on II–VI group semiconductor materials have been reported. Generally, ZnS nanowire, CdS nanowire, and ZnSe nanobelt photodetectors exhibit high sensitivity and a low dark current, because of their large surface-to-volume ratio and Debye length, which are comparable to their small size.^{17–22} Compared with conventional semiconductor structures, ZnS colloidal quantum dots (QDs) display stronger absorption in the ultraviolet band, and the bandgap may be further increased due to the quantum confinement effect, rendering them much more sensitive to deep ultraviolet (DUV) light. Therefore, the ZnS QD DUV photodetector has an ultrafast response speed.²³ In addition, the large Stokes shift of Mn-doped QDs effectively avoids self-absorption. Hence, the ZnCdS:Mn QD ultraviolet panoramic imaging detector exhibits a remarkably higher detection of weak UV signals with common CCD cameras.²⁴ Meanwhile, other UVPDs based on ternary compounds have an extremely high detectivity and a lower $1/f$ noise spectral density than some GaN-based UV photodiodes.²⁵ Also, the broad range of bandgap makes II–VI group semiconductors suitable for broadband light photodetection. Based on the unique properties

of MoS₂, such as high carrier mobility and excellent light absorption extending from the visible region to the near-infrared ray (NIR) region, photodetectors using hybrids of ZnS–MoS₂ showed a broad-spectrum response (from UV to NIR).²⁶ The CdS nanorod array/reduced graphene oxide (rGO) thin film heterojunction photodetector exhibited an ultrabroadband self-powered photoresponse from the UV region to the IR region (365–1450 nm).²⁷ Fig. 1 shows the applications of UVPDs based on II–VI group semiconductors. These high-performance devices evince great advantages as the fundamental components of photosensitive units in optoelectronics and provide opportunities for the large-scale and integrated production of the ultraviolet imaging system, which will contribute to its application in many fields, such as artificial intelligence, fire detection, industrial automatic control, and astronomy.

This review is primarily focused on UVPDs based on II–VI group semiconductors. The device geometry based on II–VI group semiconductors mainly includes photo-conductive type,^{19,43–57} heterojunctions,^{10,52,58–62} and phototransistors^{62–64} (Fig. 2). Due to the sharp difference in the device configuration, these devices display completely different device performance (*e.g.*, phototransistors have higher responsivity and a faster response speed, and heterostructures and small-sized photoconductors exhibit a faster response speed). Therefore, we outline various device structures and working principles of UVPDs based on II–VI group semiconductors. In the first section, the research background of UVPDs

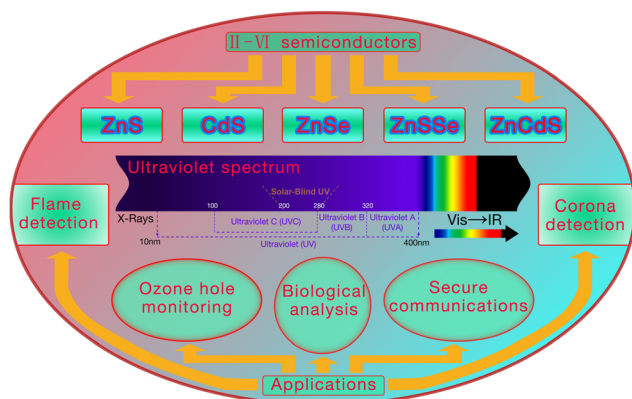


Fig. 1 Applications of UVPDs based on II–VI group semiconductors.

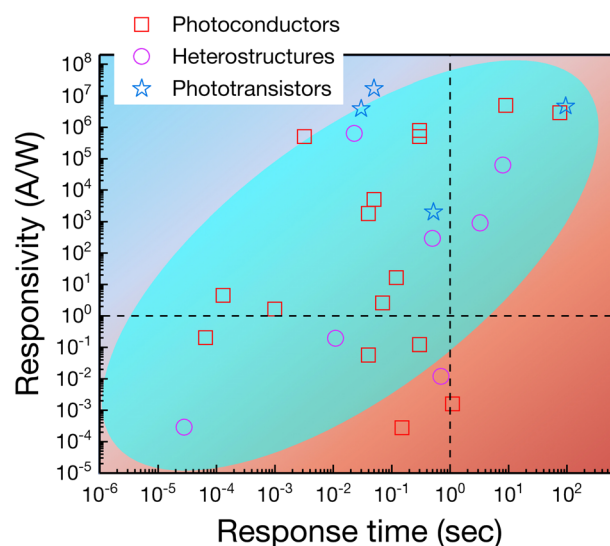


Fig. 2 A summary of the relationship of responsivity versus the response speed of different types of II–VI group semiconductor-based photodetectors.

and the research situation based on II–VI group semiconductors are introduced. The performance parameters (e.g., responsivity, quantum efficiency, and response time) and several common device structures (photoconductors and Schottky photodiodes) of UVPDs will be introduced. Then, the status of research into the main applications of UVPDs based on II–VI group semiconductors is briefly discussed. In the last section, a brief summary, possible challenges, and opportunities in the future development are provided.

2. Basics and device geometries of photodetectors

2.1 Basic parameters of UV photodetectors

Photodetectors are semiconductor devices that convert an incident light signal into an electrical signal and output it in the form of a photocurrent. When incident photons have an energy higher than the bandgap energy of the semiconductor, the electrons in the semiconductor will absorb this part of the energy and move freely in the crystal, thus changing the conductivity of the semiconductor. After an electron transitions, it leaves a vacancy called a hole. The electron and vacancy are referred to as electron–hole pairs. In an ideal situation, one electron–hole pair is created for every photon absorbed by the crystal. The drift of electron–hole pairs will generate a drift current in the semiconductor, and this part of the current is detected in the external circuit. Depending on the absorption of light by semiconductor materials, the detection wavelengths of photodetectors may cover from the ultraviolet region to the infrared spectral region. After a long-term exploration of photodetectors, researchers have developed a set of mature device performance indicators for evaluation. These parameters include the light/dark current, responsivity, external quantum efficiency, response time, photoconductive gain, detectivity, and noise equivalent power. These parameters indicate how the detector responds, as shown below.

Light/dark current. A photocurrent is generated by excitation with incident light. If photon absorption occurs in the depletion layer, the built-in electric field in this region will remove the potential barrier, causing holes to move to the anode and electrons to the cathode to form a photocurrent. A dark current is a very small current that is still generated by the device when no photons pass through the photodetector (e.g. photomultiplier, photodiode, and CCD), namely, the reverse saturation current of the device. A dark current is generally caused by the diffusion of carriers or surface and internal defects in the device. To obtain the photoelectric device with a high signal-to-noise ratio, the dark current should be controlled to as low a level as possible to obtain a photoelectric device with a high signal-to-noise ratio.

Quantum efficiency. The quantum efficiency is the probability of incident photons generating charge carriers in the photodetector, which is defined as the ratio of the number of electron–hole pairs collected by the photodetector to the number of incident photons,⁶⁵

$$\eta = \frac{I_{\text{ph}}}{q\Phi} = \frac{I_{\text{ph}}h\nu}{qP_{\text{opt}}} \quad (1)$$

where I_{ph} is the photocurrent, Φ is the incident light flux ($= P_{\text{opt}}/h\nu$), and P_{opt} is the incident optical power. The ideal value of the quantum efficiency is 1. In practice, factors such as the incomplete absorption of incident light and carrier recombination will result in a decrease in the quantum efficiency.

Responsivity. Photoelectric responsivity is one of the critical parameters used to evaluate the sensitivity of a photodetector and is defined as the photocurrent per unit of the incident optical power at a specific wavelength (λ):^{56,66}

$$R = \frac{I_{\text{ph}}}{P_{\text{opt}}} = \frac{\eta q}{h\nu} = \frac{\eta\lambda \text{ (nm)}}{1240} \text{ (A W}^{-1}\text{)} \quad (2)$$

Some devices will introduce an internal gain mechanism to improve the responsivity of the device. The gain is equal to the number of electrons passing through the photodetector per excitation or absorbed photons.⁶⁷ When the incident light wavelength λ is determined, the high responsivity of the devices is attributed to the quantum efficiency and photoconductive gain (g), and the responsivity is calculated as follows:

$$R_i = \frac{\lambda\eta}{hc} qg \quad (3)$$

where h is Planck's constant, c is the light velocity, and q is the electron charge. The gain depends on the carrier lifetime and transit time. Increasing the lifetime of carriers is beneficial to increasing the gain.

Response time. This parameter is used to describe the response speed of the photodetector to the transient input signal. The rise time τ_r and decay time τ_d are defined as the time when a photocurrent increases from 10% to 90% and decreases from 90% to 10% of the maximum value, respectively. The bandwidth is defined as the input optical modulation frequency at which the photocurrent is 3 dB lower than the continuous wave response. The response speed of the photodetector is limited by the time constant τ that is determined by the junction capacitance C and the load resistance R . In this case, the bandwidth is calculated using the following formula:⁶⁸

$$\text{BW} = \frac{1}{2\pi\tau} = \frac{2.20}{2\pi\tau_d} = \frac{2.20}{2\pi\tau_r} \quad (4)$$

Noise equivalent power and detectivity. Photodetectors also generate various forms of noise when they produce a strong optical response signal. The noise current determines the minimum detectable signal strength of the device. Shot noise arises from the statistical randomness of the thermal excitation of electron–hole pairs, which is particularly important for the detection of a low light intensity. The shot noise is related to the dark current (I_d) and bandwidth (B) as follows:⁶⁹

$$i_{\text{shot}} = (2qI_dB)^{1/2} \quad (5)$$

Reducing the dark current and increasing the system bandwidth may effectively suppress the shot noise. Another type of noise is the thermal noise (Johnson noise), which was first

confirmed by Johnson in 1928. This form of noise exists in all resistive materials, is generated by the constant random motion of the carriers, and occurs in the absence of any voltage bias. The short circuit noise current is given by⁷⁰

$$i_{\text{Johnson}} = \left(\frac{4k_{\text{B}}TB}{r} \right)^{1/2} \quad (6)$$

where k_{B} is the Boltzmann constant, T is the temperature, and r is the resistance in the circuit. A feasible approach to obtain photodetectors with higher performance is to couple a larger load resistance in the external circuit to reduce the Johnson noise. In addition, the optical and thermal generation and recombination of electron–hole pairs in semiconductors will cause the generation–recombination (G–R) noise,

$$i_{\text{G-R}} = \frac{2I_{\text{B}}}{N} \left(\frac{p\tau B}{1 + \omega_2\tau_2} \right)^{1/2} \quad (7)$$

where N and P are the electron and hole concentrations, I_{B} is the current, and τ is the carrier lifetime. The other type is the flicker noise, also known as $1/f$ noise.⁷¹ Photodetectors generally operate at high frequencies (> 1000 Hz) to reduce $1/f$ noise. The total noise of the photodetector is

$$i_{\text{noise}}^2 = i_{1/f}^2 + i_{\text{shot}}^2 + i_{\text{G-R}}^2 + i_{\text{Johnson}}^2 \quad (8)$$

All noise in the device is independent, and its associated figure of merit is the noise equivalent power (NEP), which indicates that, when the incident radiation is weak, the generated voltage signal is difficult to distinguish. At this time, the incident radiation power is the minimum optical power detected by the photodetector. Namely, a smaller P_{min} results in a stronger detection ability of the device.⁷² The reciprocal of the NEP is the detectivity, which is normalized to the area of device A , and D^* is defined as follows:^{73,74}

$$D^* = \frac{(AB)^{1/2}}{\text{NEP}} = \frac{R(AB)^{1/2}}{I_{\text{n}}} \quad (9)$$

where I_{n} is the noise current generated by the carrier generation and recombination process and D^* is a measure of the inherent detection capability of the material.

2.2 Classification of UV photodetectors

According to previous reports, numerous types of device structures involving photoconductors, p–n photodiodes, Schottky photodiodes, and heterojunction have been developed for UVPDs. Fig. 3 shows the schematic diagrams of several common device structures. UVPDs with different structures have significant differences in fabrication costs and application environments, and corresponding device performances are also quite distinct. In this section, we classify UVPDs based on their device structures and working principles.

(1) Photoconductors. The photoconductive detector (also named the photoconductor) is essentially a photoresistor. The operation of a photoconductor is shown in Fig. 3a. The device structure is composed of a semiconductor and ohmic contact

electrodes at both ends. The working principle is that the semiconductor absorbs photons with an energy ($h\nu$) larger than the bandgap of the material and generates electron–hole pairs, thereby changing the conductivity of the semiconductor (Fig. 3e). The conductivity of semiconductors depends on the electron and hole concentrations (n and p), i.e. $\sigma = e(\mu_{\text{e}}n + \mu_{\text{h}}p)$, where μ_{e} and μ_{h} are the electron and hole mobilities, respectively. In the dark, only a small current (dark current) flows across the channel under a bias voltage due to material defects and the effect of the device fabrication processes. Here, the conductivity is the dark conductivity, and the electron and hole concentrations are the equilibrium carrier concentrations (n_0 and p_0). Upon illumination, the electron–hole pairs generated by the absorption of photons by the semiconductor are separated under the action of the external electric field, and the free electrons and the holes drift in the opposite direction of the electrode. The electrodes mainly use ohmic contacts to facilitate the entry of carriers into the external circuit through the device. Typical I – V curves of the photoconductors are displayed in Fig. 3i. The ohmic contact does not have a barrier during the electron transit.⁷⁵ The conductivity at this time is mainly contributed by the excess carriers generated by illumination:

$$\Delta\sigma_0 = \sigma - \sigma_0 = e(\mu_{\text{e}}\Delta n + \mu_{\text{h}}\Delta p), \quad (10)$$

where $\Delta n = n - n_0$ and $\Delta p = p - p_0$ are the photogenerated electron and hole concentrations, respectively. Depending on the production processes of the photogenerated carriers, two principal types of photoconductivity have been identified: intrinsic photoconductivity and extrinsic photoconductivity. The intrinsic photoconductivity is attributed to the excess electrons and holes that are generated by the band-to-band absorption of incident photons. The extrinsic photoconductivity is attributed to the carriers that are generated by optical transitions associated with impurity levels within the bandgap of an extrinsic semiconductor. As a result of the effect of electron and hole lifetimes and the time of the transition between electrodes, a photoconductive gain is often observed in the carrier transport process. The carrier lifetime should be sufficiently long and the electrode spacing should be reduced to obtain a high gain. On the other hand, the response time of the photoconductivity depends on the carrier lifetime, and thus a high gain and fast response speed are difficult to achieve simultaneously. Moreover, the minority carrier sweep-out may also improve the gain. In the presence of a low electric field, the majority carriers (electrons) have higher mobility and their transit time is shorter than the carrier lifetime. The minority carriers (holes) are slower and their transit time is longer. Accordingly, electrons are swept out of the device quickly, while more holes are still located inside. At this point, more electrons from the other electrode are needed to maintain an electrical neutrality. This device has the advantages of simple fabrication, low cost, and robustness. The device typically has a high gain but a slow response time and large dark current. However, large photoconductivity gains are usually accompanied by persistent photoconductivity (PPC) due to the trapping of the minority carriers by defect states, which results in a slow recovery rate.^{76,77}

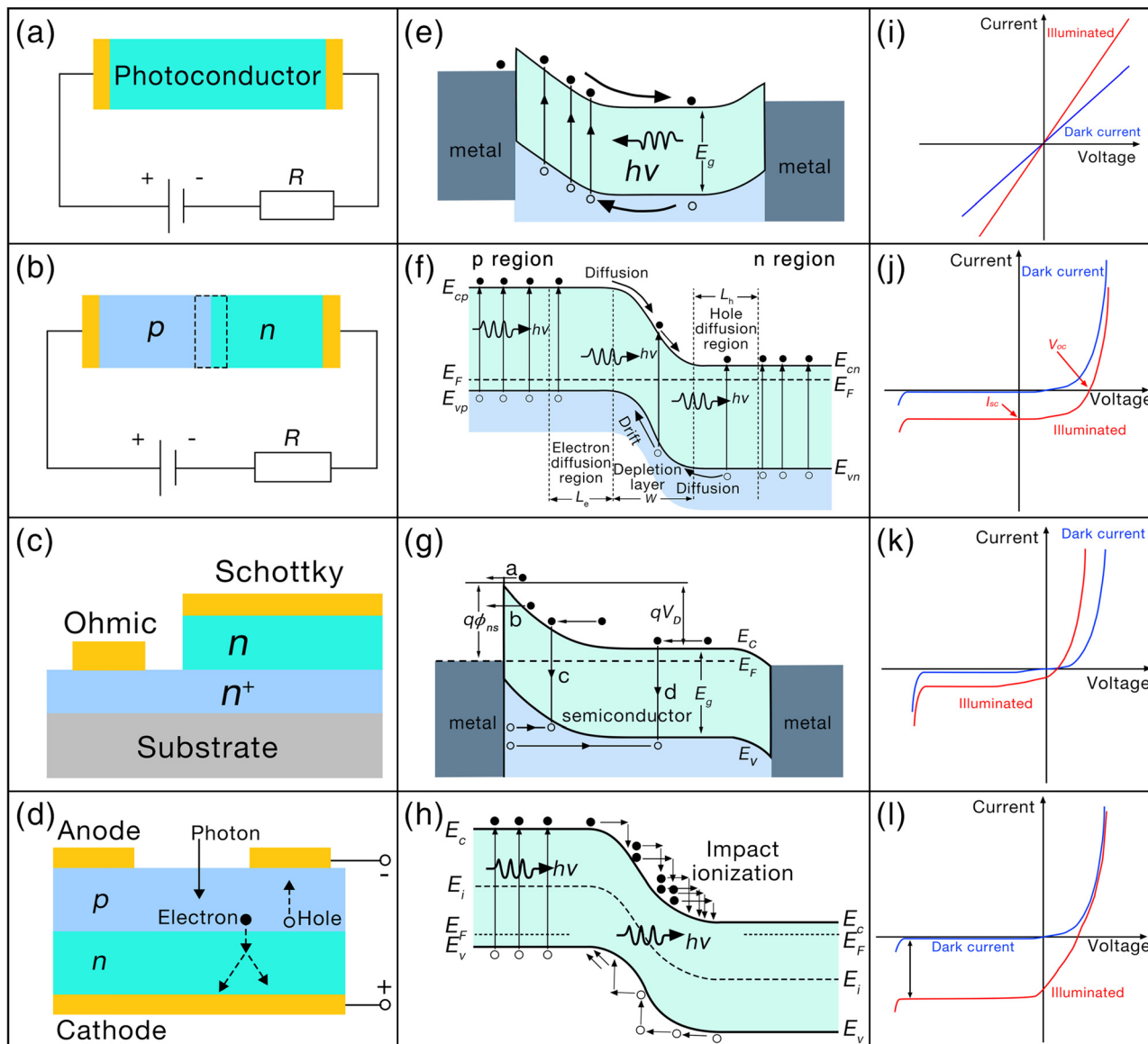


Fig. 3 Schematic illustration of device architectures of (a) photoconductors, (b) p-n junction, (c) Schottky junction, and (d) avalanche photodiodes. Schematic of the corresponding (e-h) energy band diagrams and (i-l) I - V characteristics.

The PPC is a light induced change in free carrier concentrations that persists after photoexcitation has been removed. In general, the PPC is attributed to a bistable defect existing between a shallow energy state and a deep energy state.^{78,79}

(2) p-n junction, heterojunction. A p-n junction photodetector is usually a junction created by the combination of two semiconductors of opposite doping types (Fig. 3b). The primary mechanism is the photovoltaic effect. Because of the carrier concentration gradient in the two semiconductors with different doping types, the electrons and holes diffuse to form a space charge region. These charges in the space charge region generate a built-in electric field. The effect of the built-in electric field is to cause charges with opposite signs to move in opposite directions according to the external circuit. Upon illumination, photons with energies higher than the semiconductor bandgap are

absorbed, creating electron-hole pairs on both sides of the junction, as shown in Fig. 3f. Electrons and holes within the diffusion length of the p-n junction are transported to the space charge region and separated by the built-in electric field. The minority carriers are easily accelerated to the majority carriers on the other side. The movement of photogenerated electron-hole pairs in the p-n junction increases the potential of the p region. This process is equivalent to applying a forward bias voltage V on the p-n junction, which reduces the p-n junction barrier from qV_D to $qV_D - qV$. Meanwhile, this forward voltage also causes the current $I_d = I_{s0}(\exp(eV/kT) - 1)$ to flow through the p-n junction, and the direction of I_d is opposite to the direction of the photocurrent I_p . Fig. 3j shows the I - V characteristics of a p-n junction photodetectors. Therefore, the total current of the p-n junction under the action of incident light is expressed as follows:¹⁴

$$I(V) = I_{s0}[\exp(qV/kT) - 1] - I_p \quad (11)$$

where I_{s0} is the saturation current, V is the applied voltage, k is the Boltzmann constant, and T is the temperature.

Similar to the p-n junction, the heterojunction consists of two different semiconductor materials. On account of the difference in the carrier concentration and Fermi level in the two materials that compose the heterojunction, the Fermi level will be flat due to the carrier diffusion after the contact, and this diffusion will also form a built-in electric field at the interface of the heterojunction.⁸⁰ The heterojunctions are simple to fabricate and do not need to consider doping problems related to the conductive type of materials.

(3) Schottky photodiodes. As a result of the complexity of fabricating bipolar devices and heterojunctions, other device structures are required to achieve the effective separation of charge carriers. This separation is achieved using the concept of the Schottky barrier. The device structure is similar to the p⁺-n junction (Fig. 3c). According to a simple Schottky-Mott model, the rectifying property of the device is caused by the potential barrier between the metal-semiconductor contacts, and this type of device is a majority carrier device. Taking an n-type semiconductor as an example, when the metal and semiconductor are in contact, the interface characteristics mainly depend on the work function of a metal and a semiconductor (ϕ_m and ϕ_s). If $\phi_m > \phi_s$, the electrons flow from the semiconductor to the metal, and the surface negative charge density on the metal side increases, while the surface positive charge density on the semiconductor side increases.⁸¹ Consequently, an electric field is formed in the semiconductor, resulting in energy band bending. Schottky barriers with heights of $qV_D = \phi_m - \phi_s$ and $q\phi_{ns} = \phi_m - \chi_s$ are formed on the semiconductor side and the metal side, respectively. If $\phi_m < \phi_s$, the electrons flow from the metal to the semiconductor side and the metal-semiconductor junction forms an ohmic contact and a high conductivity region without a Schottky barrier. The light absorption of Schottky diodes occurs in the thinner junction region, and the majority carriers (electrons) in n-type semiconductors drift through the active region and are not affected by the accumulation of minority carriers; therefore, the Schottky diodes usually have a faster response speed.^{82,83}

In contrast to the p-n junction, in Schottky diodes, the current transport in metal-semiconductor contacts is dominated by the majority of carriers. Fig. 3g shows the four transport processes of electrons across the metal-semiconductor junction:^{84,85} (a) emission of electrons from the semiconductor over the top of the barrier into the metal, (b) quantum mechanical tunneling through the barrier, (c) recombination in the space-charge region, and (d) recombination in the neutral region (metal to semiconductor hole injection).

In practical device fabrication, for impure semiconductor devices with high mobility, the thermionic emission theory qualitatively explains the I - V characteristics of the device.^{86,87} In Bethe's thermionic emission theory,⁸⁸ the potential barrier height is first assumed to be much larger than kT . Furthermore, the thermal equilibrium has been established at the plane that determines the emission. Finally, the existence of a net current

flow does not affect this equilibrium, and thus the two current fluxes may be superimposed (one from the metal to the semiconductor ($J_{m \rightarrow s}$) and the other from the semiconductor to the metal ($J_{s \rightarrow m}$)). The width of the depletion layer is expressed as follows:⁸⁹

$$W_D = [2\epsilon_s(V_{bi} - V - kT/q)/qN_D]^{1/2} \quad (12)$$

where ϵ_s is the permittivity of the semiconductor, V_{bi} is a built-in potential barrier on the semiconductor side, and N_D is the donor concentration. The equation for the current density under the dark condition is written as follows:⁹⁰⁻⁹²

$$J_n = J_{s \rightarrow m} + J_{m \rightarrow s} = J_{ST} \left[\exp\left(\frac{qV}{kT}\right) - 1 \right] \quad (13)$$

where the saturation current density is

$$J_{ST} = A^* T^2 \exp\left(-\frac{q\phi_{ns}}{kT}\right) \quad (14)$$

where A^* is the effective Richardson constant for the thermionic emission ($A^* = 4q\pi m^* k^2/h^3$), and m^* is the effective mass of the electron. The barrier height that electrons must cross from the metal to the semiconductor does not vary with the applied voltage. Thus, $J_{m \rightarrow s}$ is a constant and is not affected by the applied voltage. Eqn (13) is similar to the transport equation for the p-n junction, but the equation for the saturation current density is quite different. Based on eqn (14), the saturation current density J_{ST} is very sensitive to temperature. Compared with the thermionic emission theory, the diffusion theory applies to low-mobility semiconductors, and its equation is very similar to the thermionic emission theory. However, a difference in the saturation current density is noted as follows:^{88,93}

$$J_{SD} = \frac{q^2 D_e N_c}{kT} \left[\frac{q(V_{bi} - V) 2N_d}{\epsilon_0 \epsilon_s} \right], \quad (15)$$

where D_e is the diffusion coefficient, N_c is the density of states in the conduction band, and N_d is the donor density. Compared with the saturation current density J_{ST} of thermionic emission theory, J_{SD} is more dependent on the voltage variation and less sensitive to the temperature. However, surface states and defect state-induced trapping states exist at the Schottky contact interface, and these traps are negatively charged.⁹⁴ Under illumination, the photogenerated holes generated in the depletion region drift toward the metal-semiconductor interface due to band bending and are trapped by the traps, producing net positive charges of $Q_{ss} = qN_{ss}$. The metal negative charges Q_m and the positive charges Q_d in the depletion region satisfy the neutrality condition of $Q_{ss} + Q_m + Q_d = 0$. As a result, the reduction of the amount of band bending $V_{bi-\lambda}$ will follow the relationship $V_{bi-\lambda} = V_{bi-d} - W_D/2\epsilon_0\epsilon_s$,^{95,96} where V_{bi-d} is the barrier height under the dark condition, and W_D is the width of the depletion region.⁹⁵ The reduction of V_{bi} under illumination will lead to a reduction of the Schottky barrier height $q\phi_{ns}$, namely $\Delta q\phi_{ns}$. Thus, the current obtained under illumination is as follows:^{95,97}

$$J_i = \exp\left(\frac{\Delta q\phi_{ns}}{kT}\right) J_n - J_\lambda \quad (16)$$

where the photocurrent J_{λ} does not depend on the photoconductive gain, and arises from the photon-generated electron-hole pairs in the depletion layer. The typical I - V curves of the Schottky photodiodes are shown in Fig. 3k.

(4) Avalanche photodiodes. Avalanche photodiodes (APDs) mainly use carriers to generate avalanche multiplication under a sufficiently large reverse bias. After the incident photon is absorbed, an electron-hole pair is generated and separated to both sides of the diode (Fig. 3d). When transported to the electrode, the charge carriers acquire a sufficient speed to generate additional electron-hole pairs from the lattice by impact ionization. The number of generated charge carriers increases exponentially with the distance (Fig. 3h). Devices tend to operate at higher electric fields. The effectiveness of the APDs is determined by the avalanche gain, which is defined as the ratio of the photocurrent with and without amplification. Therefore, the APDs usually exhibit a huge photo-dark current ratio (Fig. 3l). The avalanche photodiodes generally have the advantages of a fast response, high sensitivity, and large current gain. However, the high gain often occurs at the expense of the increased noise.

3. II-VI group semiconductor based UV photodetectors and applications

II-VI group semiconductor materials have attracted extensive attention due to their excellent optoelectronic properties.

Another important characteristic of II-VI group semiconductors is the direct bandgap structure; namely, in quasi-momentum space, the maximum of the valence band coincides with the minimum of the conduction band. This property opens up greater possibilities for building optoelectronic devices in the visible to ultraviolet range. In the past few years, great progress has been achieved in the development of high-performance UVPDs based on different structures of II-VI group semiconductors (e.g., zero-dimension (0D), one-dimension (1D), two-dimension (2D), and so on).

3.1 0D nanostructured materials for photodetectors

0D nanostructures generally refer to materials whose excitons are confined in all three spatial dimensions (<100 nm). The nanoscale confinement of 0D materials makes their bandgap achievable by tuning their size and shape. In addition to the tunable bandgap, the relatively large specific surface area enables 0D materials to have a higher light absorption efficiency. Therefore, 0D materials can be combined with other semiconductors to achieve high-performance UVPDs. Many novel UVPDs have been proposed based on 0D II-VI group semiconductor materials in recent years. Hu *et al.* developed a high-performance UVPD based on ZnS and ZnO hollow microspheres, whose performance is comparable to that of commercial GaN-based UVPDs.⁹⁸ Moreover, graphene field effect transistors (FETs) are covered with a layer of CdS nanocrystals by a simple spin coating, which greatly enhances their absorption in the UV region.⁹⁹ Photodetectors based on colloidal quantum dots

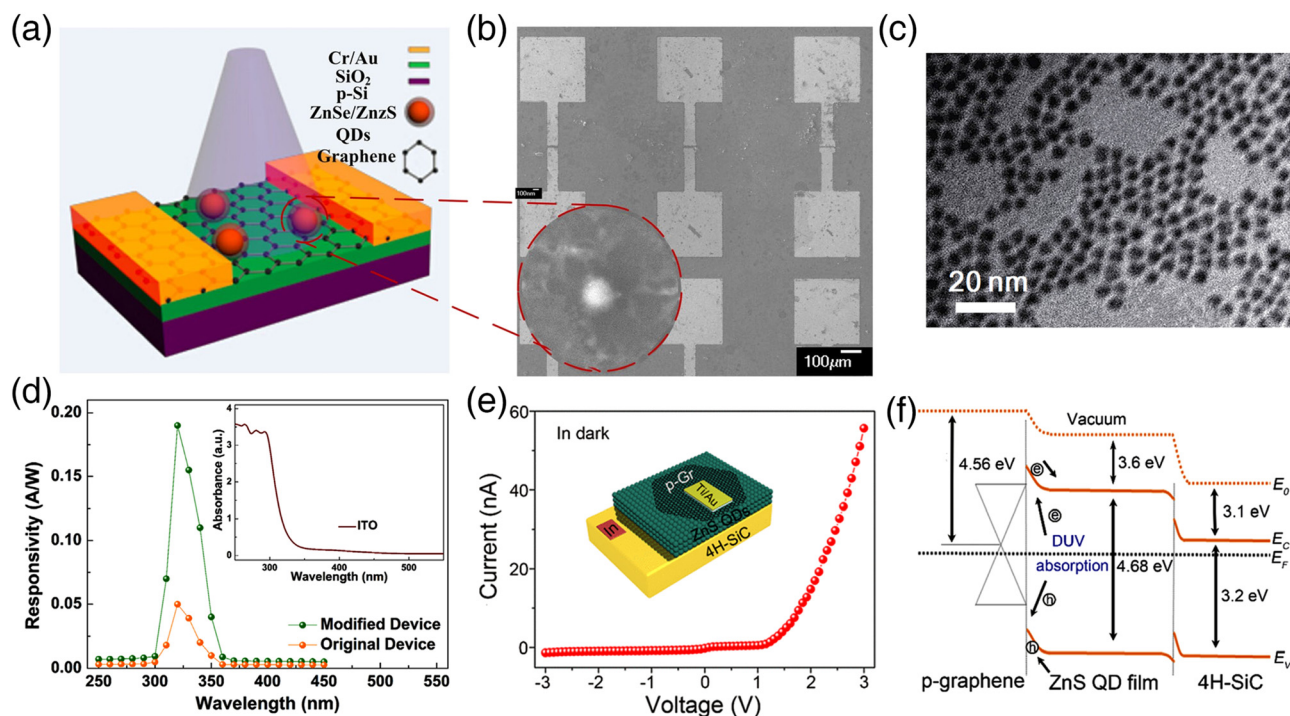


Fig. 4 (a) Schematic illustration of a graphene FET decorated with ZnSe/ZnS QDs under illumination. (b) SEM image of device arrays on the graphene films. Reproduced with permission from ref. 62. Copyright 2018, Springer Nature. (c) TEM image of CuInS₂/ZnS quantum dots. (d) The responsivity of the modified device and original device under UV illumination at a bias of 1 V and the inset is the absorbance of the ITO substrate. Reproduced with permission from ref. 61. Copyright 2018, Elsevier. (e) I - V curves of the device in the dark. Inset: The schematic image of the device. (f) Energy band diagram of the p-type graphene/ZnS QD film/4H-SiC heterostructure. Reproduced with permission from ref. 23. Copyright 2019, American Chemical Society.

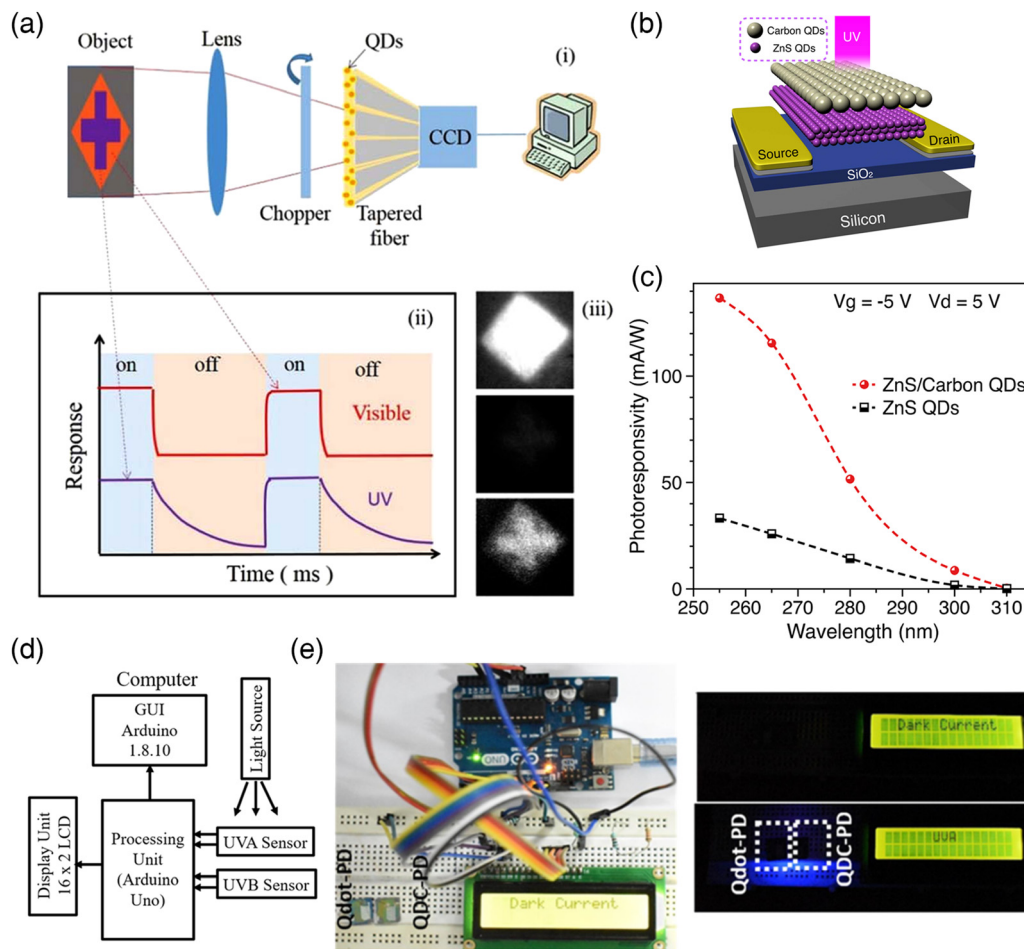


Fig. 5 (a) Schematic illustration of the single-channel UV panoramic detection system and photographic images detected using the visible CCD camera. Reproduced with permission from ref. 24. Copyright 2018, IOP Publishing. (b) Schematic illustration of the phototransistor. (c) Photoresponse performance of bare ZnS and ZnS/carbon QD phototransistors. Reproduced with permission from ref. 103. Copyright 2020, IEEE. (d) Block representation of the connection of the sensors to Arduino UNO and (e) photograph of the integrated device. Reproduced with permission from ref. 55. Copyright 2022, American Chemical Society.

(QDs) are technologically attractive, as they can be fabricated using low-cost room-temperature growth methods and are compatible with various substrates.^{100–102} The devices can be made by depositing the solution through spin coating or spray coating. Kuang *et al.* reported solar-blind photodetectors by using ZnS QDs as building blocks.⁴⁵ The cubic ZnS QDs have an average particle size of ~ 2.29 nm, with a bandgap of 4.11 eV. The responsivity of the device is found to increase linearly from 300 to 254 nm. In addition, photodetectors prepared by decorating monolayer graphene with ZnSe/ZnS core/shell QDs *via* a simple solution method have been reported as well (Fig. 4a).⁶² As shown in Fig. 4b, the graphene FET channel with single ZnSe/ZnS QDs in a spheroidal shape exhibited very good sensitivity to UV light with a responsivity as high as 10^3 A W⁻¹. In addition, Xu *et al.* reported a high-performance photovoltaic UVPD made of a polyvinyl carbazole (PVK)/TiO₂ heterojunction with CuInS₂/ZnS quantum dots (CIS-Z QDs) doped in the PVK layer (Fig. 4c).⁶¹ Due to the quantum size effect of CIS-Z QDs, the electric field intensity in the depletion of the device is enhanced, and the responsivity has also been improved (Fig. 4d). In 2019,

Kan *et al.* constructed a hybrid zero-/two-dimensional DUV photodetector (p-type graphene/ZnS QDs/4H-SiC) with a photovoltaic effect.²³ The *I*-*V* curve of the device in the dark is shown in Fig. 4e. Due to the PIN-type photodiode formed by p-type graphene, the ZnS QD film, and the 4H-SiC substrate, the device exhibits excellent rectification characteristics, and the dark current of the device is 55.64 nA at 3 V. The responsivity of the device is 0.29 mA W⁻¹ at a wavelength of 250 nm, indicating that the photodetector can be used in the field for DUV detection. In this device, a built-in electric field is formed at the interface between the p-Gr and the ZnS QD films at a bias of 0 V. Under 250 nm illumination, the electron-hole pairs generated in the ZnS QD film are separated by the built-in electric field, where the holes drift toward the graphene surface, and the electrons move toward 4H-SiC (Fig. 4f). For this vertical structure device, the carrier transit time is much shorter than the electron and hole recombination time, leading to a relatively fast DUV photoresponse time.

Yuan *et al.* fabricated a single-channel UV/vis dual-band detector based on ZnCdS:Mn/ZnS QDs and applied it to a

Si-based CCD camera, which improved the detection efficiency of the visible CCD camera for a weak UV signal in a strong visible light background.²⁴ Fig. 5a shows the schematic diagram of the signal-channel panoramic UV detection system proposed by the research group. In this imaging system, the optical signals mixed with UV and visible light reach the visible

CCD camera through the optical fiber, and then a new image is formed in the signal processing unit. The chopper is used to control the on/off state of the optical channel. Due to the long PL lifetime of Mn-doped QDs, the CCD still captures the residual fluorescence of the UV signal when the optical channel is closed. When the optical channel is open, both the visible

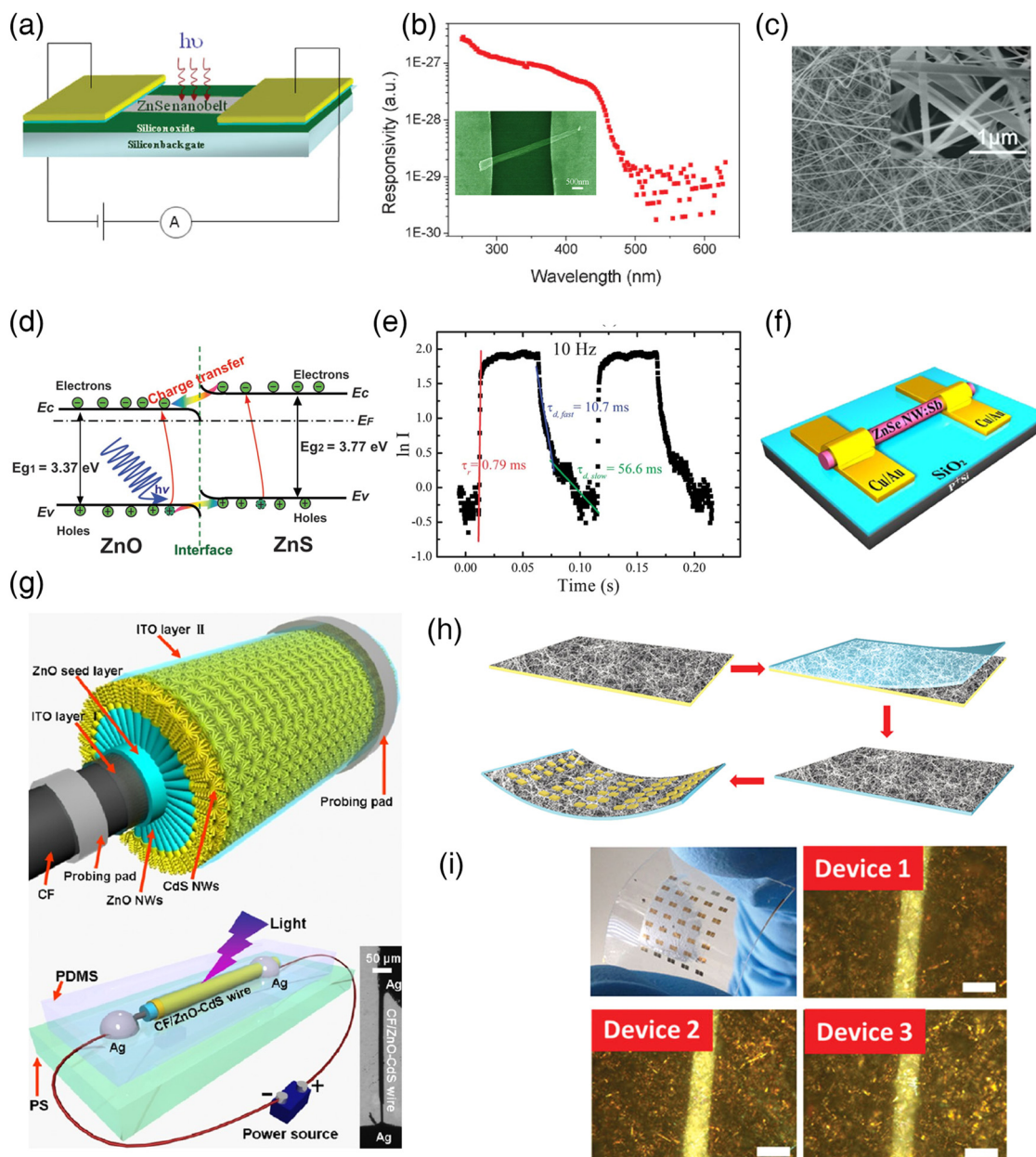


Fig. 6 (a) A schematic illustration of a photodetector based on a single-crystal ZnSe-nanobelt. (b) A spectral photoresponse of the device was measured at a bias of 30 V. The inset shows the SEM image of a single-crystalline ZnSe nanobelt photodetector. Reproduced with permission from ref. 19. Copyright 2009, John Wiley and Sons. (c) SEM image of the ZnS:Sb NRs. Reproduced with permission from ref. 83. Copyright 2011, AIP Publishing. (d) Schematic energy band diagram of the photodetector based on a ZnS/ZnO biaxial nanobelt with Cr/Au electrodes. Reproduced with permission from ref. 44. Copyright 2012, John Wiley and Sons. (e) The $I-t$ curves of the individual ZnS nanowire photodetector under 325 nm light illumination. Reproduced with permission from ref. 18. Copyright 2012, Royal Society of Chemistry. (f) Schematic illustration of the back-gate ZnSe NW FET. Reproduced with permission from ref. 20. Copyright 2013, IOP publishing. (g) Schematic representation of the fabrication of a single carbon-fiber/ZnO-CdS nanowire-based photodetector. Reproduced with permission from ref. 7. Copyright 2013, American Chemical Society. (h) Schematic diagram of the ZnS nanowires transferred onto the PET substrate and their overall device structure. (i) An optical image of the ZnS-ZnO devices on a PET substrate and micrographs of three as-fabricated devices. Reproduced with permission from ref. 105. Copyright 2014, John Wiley and Sons.

signal and the UV signal reach the maximum values. The image from the signal processing unit is obtained by integrating the electrical signals detected in a certain period. Finally, by integrating the control circuit, signal recognition, and image processing software, the UV/visible dual-band detection is achieved. In addition, QD-based heterostructures and hybrid structures have also been demonstrated to realize solar-blind phototransistors. In 2020, solar-blind ZnS/carbon QD heterojunction phototransistors were reported (Fig. 5b).¹⁰³ It is revealed that the as-fabricated phototransistors display superior photodetection capability, in comparison with the ZnS QD device (Fig. 5c), which is attributed to the stronger carrier separation at the heterojunction interface. Gogoi *et al.* fabricated photodetectors in the UVC and UVA regions based on the surface engineering of Mn²⁺-doped ZnS QDs.⁵⁵ It is interesting to find that the as-fabricated device can be integrated into a portable prototype to demonstrate their potential applications for UVC and UVA spectral detection (Fig. 5d). In this prototype device, the detectors were connected through a voltage divider circuit to the controller unit, and the real-time detection of UV radiation was achieved (Fig. 5e).

3.2 1D and 2D nanostructure based photodetectors

1D nanostructured materials, such as nanowires and nanotubes, have attracted great research interest in recent years due to their unique properties and potential in the field of nanotechnology. Compared with 2D nanostructured materials, 1D nanostructured materials possess an additional spatial dimension (in total 2 dimensions confined within the nanoscale). In addition, the large specific surface area and the Debye length of 1D nanostructures make photodetectors based on 1D nanostructures one of the most attractive optoelectronic devices in recent years. Compared with conventional epitaxial growth techniques for semiconductor thin films, the preparation methods of 1D and 2D nanostructured materials are generally simpler and, most importantly, at a lower cost. Their rich physical properties and other characteristics play an important role in the construction of photoelectric functional devices. Fang *et al.* fabricated single-crystalline zinc selenide (ZnSe) nanobelts using the ethylenediamine (en)-assisted ternary solution technique and subsequent thermal treatment.¹⁹ The nanobelts have a uniform thickness (~40 nm). Then, individual ZnSe nanobelts were assembled into UVPDs (Fig. 6a). In addition, the device exhibits a high spectral photoresponse at a bias of 30 V (Fig. 6b). Moreover, this group also reported thin-film-like 'visible-blind' micrometer-scale ZnS nanobelt UV light photodetectors in 2010.¹⁰⁴ The nanobelt device derived from a CVD method exhibited a fast response speed and good stability in different measurement environments. In addition, Wei and co-worker demonstrated a Schottky contact UVPD using CdS nanowires.²² With changing one of the CdS nanowire-electrode contacts from ohmic to Schottky, detection sensitivities of the device were as high as 10⁵% at -8 V, which was 58 times higher than the corresponding ohmic contact device. In 2011, Peng *et al.* fabricated Sb-doped p-type ZnS nanoribbons by using Sb as the dopant.⁸³ The width of the nanoribbons ranges from

200 to 400 nm and the length is from tens of micrometers up to hundreds of micrometers (Fig. 6c). Nano-Schottky barrier diodes based on Al/p-ZnS nanoribbon junctions exhibited excellent device performances with a high rectification ratio of >10⁷. Furthermore, the conductivity of ZnS nanoribbons can be significantly improved by Cl doping and could be tuned over a wide range of 3–4 orders of magnitude by adjusting the Cl doping level.⁴³ Notably, the photoconductive gain of ZnS:Cl NR photodetectors can be as high as ~10⁷. Hu *et al.* fabricated UVPDs with tunable spectral selectivity and a wide-ranging photoresponse based on ZnO/ZnS biaxial nanobelts.⁴⁴ The device exhibits higher spectral selectivity and a fast response speed, which is much better than that of pure ZnO or ZnS nanostructures. Notably, a good ohmic contact between the ZnS/ZnO nanobelts and the Cr/Au electrodes is observed. The responsivity and external quantum efficiency of the device is 5 × 10⁵ A W⁻¹ and 2 × 10⁸%, respectively. The spectral response is enhanced from 348 to 400 nm and 300 to 348 nm, corresponding to the intrinsic absorptions of ZnO and ZnS, respectively. Fig. 6d shows the energy band diagram of the device. Under illumination, electron-hole pairs are generated. Due to the internal field, the electrons move to the ZnO side and holes move to the ZnS side. The separation of photogenerated carriers reduces the recombination of electron-hole pairs, thereby enhancing the photoresponse of the device. Similarly, Liang *et al.* developed a UVPD by using individual ZnS nanowires as building blocks which were fabricated on the n⁺ type GaAs(111) B substrate by MOCVD.¹⁸ This device has a responsivity and external quantum efficiency to the 325 nm light of 1.86 A W⁻¹ and 710%, respectively. Meanwhile, the device has a fast response speed (0.79 ms), as shown in Fig. 6e. In addition, our group used Ga, Cl, and Sb as dopants to study the effect of doping on the optoelectronic properties of ZnSe nanoribbons and nanowires.^{17,20,56} The devices based on Ga and Cl-doped ZnSe nanoribbons exhibited a high photo-to-dark current ratio and a high photoconductive gain, respectively.^{17,20} The single ZnSe:Sb nanowire based back-gate FET (Fig. 6f) displays a rectification ratio as high as 10³ at ±5 V. Moreover, the visible/UV photodetector based on the carbon-fiber/ZnO-CdS double-shell microwire was demonstrated by Zhang *et al.* in 2013 (Fig. 6g).⁷ This device exhibits an ultra-high responsivity up to 10⁵ A W⁻¹ under 372nm illumination. Tian *et al.* reported a branched architecture with ZnS backbones and ZnO branches that was prepared by combining a facile thermal evaporation process and hydrothermal growth.¹⁰⁵ ZnS-ZnO branched heterostructures were transferred onto a PET substrate, and Cr/Au electrodes were deposited to fabricate photodetector arrays (Fig. 6h). The physical image and optical micrograph of the devices are shown in Fig. 6i. The dark current of the device is as low as 5.3 pA, and this device has great potential for applications in flexible optoelectronics.

Rai *et al.* successfully fabricated a high-performance broadband UV/visible photodetector on a fully wide bandgap ZnO/ZnS type-II heterojunction core/shell nanowire array.¹⁰⁶ First, the ZnO nanowire array was synthesized through the thermal evaporation of Zn powder in a tube furnace, and then ZnS was grown using PLD to synthesize ZnO/ZnS nanowire arrays.

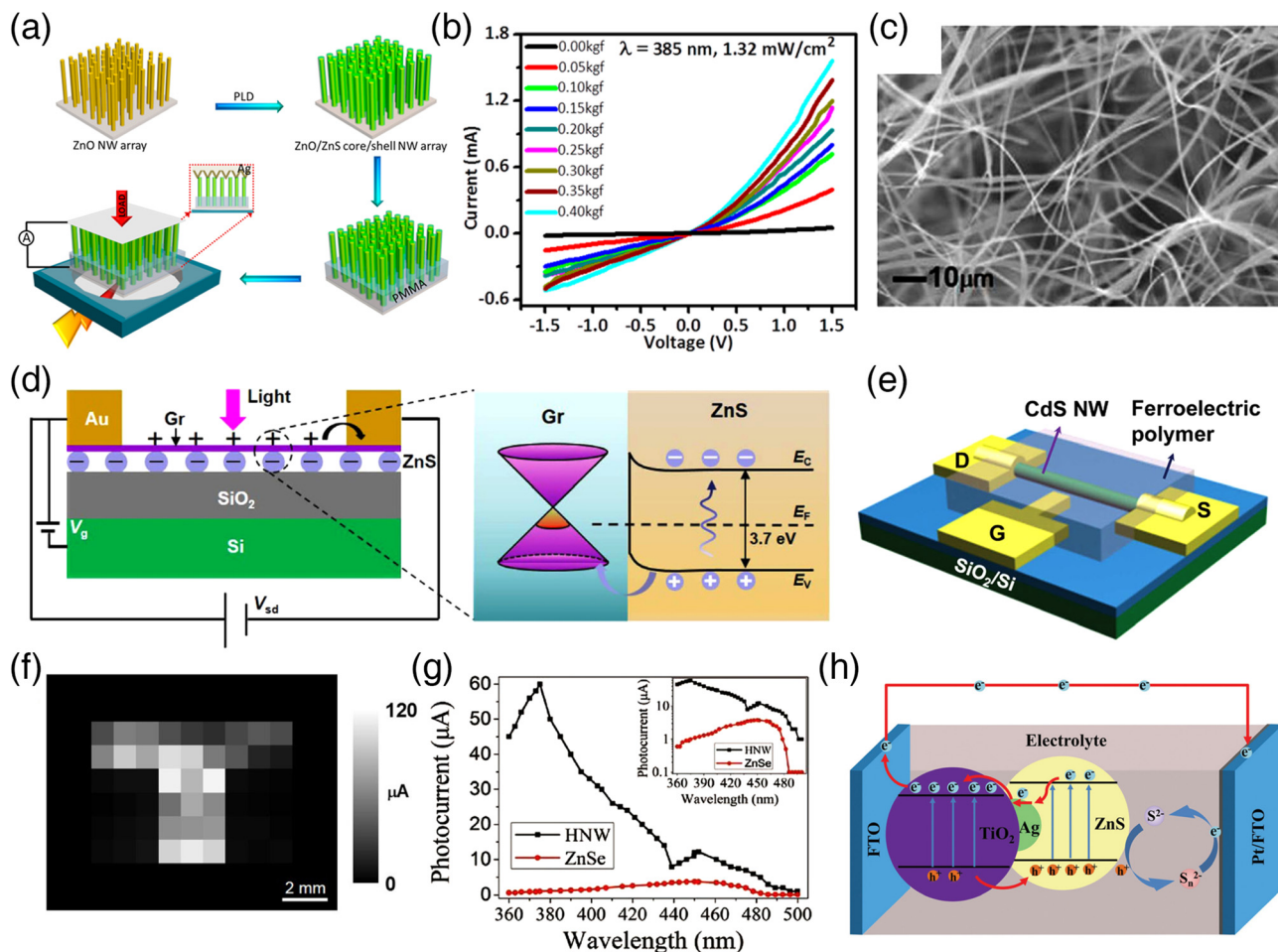


Fig. 7 (a) Schematic illustration of the fabrication process of the ZnO/ZnS core/shell nanowire photodetector. (b) Photocurrent response of the ZnO/ZnS core/shell nanowire array devices. Reproduced with permission from ref. 106. Copyright 2015, American Chemical Society. (c) A typical SEM image of ZnS:Cl nanoribbons. Reproduced with permission from ref. 81. Copyright 2015, Springer Nature. (d) Scheme for the proposed working mechanism of the device. Reproduced with permission from ref. 64. Copyright 2016, Springer Nature. (e) A schematic illustration of the ferroelectric side-gated single CdS nanowire photodetector. Reproduced with permission from ref. 108. Copyright 2016, John Wiley and Sons. (f) 2D contrast map of the photocurrent of the device. Reproduced with permission from ref. 109. Copyright 2017, IOP Publishing. (g) Wavelength-dependent photocurrent response of ZnS_{0.49}Se_{0.51}/ZnSe heterostructure nanowires and pure ZnSe nanowire photodetectors. The inset is the corresponding semilogarithmic plot. Reproduced with permission from ref. 10. Copyright 2019, John Wiley and Sons. (h) Schematic illustration of the possible charge transfer mechanism of the self-powered TiO₂/Ag/ZnS UVPD. Reproduced with permission from ref. 111. Copyright 2020, Royal Society of Chemistry.

Finally, the photodetector was fabricated by sputtering Ag on the top of the nanowire array (Fig. 7a). As shown in Fig. 7b, the peak photocurrent of the device increases when the compressive load is increased under the steady photon flow, and the maximum photocurrent (1.5 mA) is ~ 31 times higher than the photocurrent without a load (51 μA). The high performance of the device is attributed to the piezo-phototronic effect. Due to the presence of negative piezoelectric charges, the upward bending of the energy band of ZnO eliminates the potential barrier Φ that is not conducive to electron separation, enabling the quick separation of electrons and holes in ZnO and ZnS. Compared to the unstrained case, a higher photocurrent is generated at the same bias and illumination. Wang *et al.* synthesized the ZnS nanoribbons by using Cl as the dopant *via* a thermal co-evaporation method (Fig. 7c).⁸¹ The nanoribbons have an electron mobility of 64.9 $\text{cm V}^{-1} \text{s}^{-1}$ and an electron concentration of $5.7 \times 10^{17} \text{cm}^{-3}$.

Schottky barrier diodes based on the ZnS/Au junctions exhibited a rectification ratio of over 10^3 . Huang *et al.* described a graphene/ZnS film hybrid photodetector with not only high performance but also reproducible performance.⁶⁴ A schematic diagram of the device structure is shown in Fig. 7d. Upon the absorption of light with an energy larger than the ZnS bandgap, electron-hole pairs are generated in the ZnS films. The photogenerated holes are spontaneously transferred to the graphene channel, and the ultra-high carrier mobility of graphene enables large holes to drift to the electrode at an ultrafast speed, thereby substantially improving the optoelectronic performance of the device. In 2016, Lou and co-workers successfully synthesized 1D ZnS/CdS heterostructures and fabricated the high-performance UV/visible photodetectors.¹⁰⁷ This device showed excellent photoresponse properties, such as an ultrahigh $I_{\text{on}}/I_{\text{off}}$ ratio ($> 10^5$) and detectivity (2.23×10^{14} Jones) and good stability and reproducibility. In addition, ferroelectric polymer

side-gated CdS nanowire UVPDs were also reported (Fig. 7e).¹⁰⁸ The ultrahigh electrostatic field of the ferroelectric polymer depletes the intrinsic carriers within the CdS nanowire channel, thus reducing the dark current of the device. The single CdS nanowire UVPD exhibited a high photoconductive gain of 8.6×10^5 , a responsivity of $2.6 \times 10^5 \text{ A W}^{-1}$, and a detectivity of 2.3×10^{16} Jones at a low power density of 0.01 mW cm^{-2} for $\lambda = 375 \text{ nm}$. Wu *et al.* successfully developed photodetector arrays based on graphene/single-crystal ZnS nanowire film hybrids.¹⁰⁹ The device has a high photocurrent of $320 \mu\text{A}$, a high responsivity of $2.6 \times 10^6 \text{ A W}^{-1}$, and a high detectivity of 8.0×10^{12} Jones. Finally, the potential application of the device in image sensing is verified (Fig. 7f). The “T” shaped LED light source is focused above the device arrays and the output photocurrent of each device is measured. Each device is treated as a pixel, and the measured photocurrents are combined into a 2D plot to generate a “T” shaped image pattern. The letter “T” is clearly resolved. This system has great application value in large-scale imaging. As long as the channel length is scaled down, most of the photogenerated carriers quickly drift to the electrodes, effectively reducing the recombination rate of electron-hole pairs. Hence, the use of short-channel photodetectors substantially improves the performance of the device. Sub-100 nm channel length photodetectors have been achieved based on the ZnSe film/graphene hybrid by Xu *et al.* in 2018.¹¹⁰ ZnSe films with a thickness of 60 nm were deposited by the e-beam evaporation

method with standard photolithography and lift-off processes. The 70 nm-channel ZnSe film/graphene hybrid photodetector shows a fast response speed (50 ms) and an ultrahigh responsivity ($1.2 \times 10^9 \text{ A W}^{-1}$), which is 3 orders of magnitude higher than that of a 5 μm channel. Obviously, the responsivity of the device is significantly enhanced as the channel length decreases. In 2019, Mu *et al.* reported the development of a photodetector by using high-quality $\text{ZnS}_{0.49}\text{Se}_{0.51}/\text{ZnSe}$ axial heterojunction nanowires (HNWs) with a uniform diameter distribution of 50–100 nm.¹⁰ The axial $\text{ZnS}_{0.49}\text{Se}_{0.51}/\text{ZnSe}$ HNWs were synthesized using an improved two-step CVD strategy. It is found that the axial $\text{ZnS}_{0.49}\text{Se}_{0.51}/\text{ZnSe}$ HNW based photodetector exhibits a wide photo-response range of 360–480 nm (Fig. 7g), with a large R and EQE of $6.3 \times 10^5 \text{ A W}^{-1}$ and $2.08 \times 10^6\%$, respectively. In addition, the UVPD based on $\text{TiO}_2/\text{Ag}/\text{ZnS}$ nanotubes shows self-powered characteristics with high stability and a fast response.¹¹¹ In this device, TiO_2 and ZnS generated the photogenerated carriers under UV light illumination. The built-in electric field in the TiO_2 and ZnS heterojunction facilitates the efficient separation of electron-hole pairs. It is worth noting that, for this device, the Ag nanoparticles not only enhance the light absorption efficiency but also play an important role in the electron transport between TiO_2 and ZnS (Fig. 7h). Furthermore, another MSM junction photodetector based on ZnS:Mn NRs showed the solar-blind superior UV photodetection, and a fast response of 12 ms.¹¹²

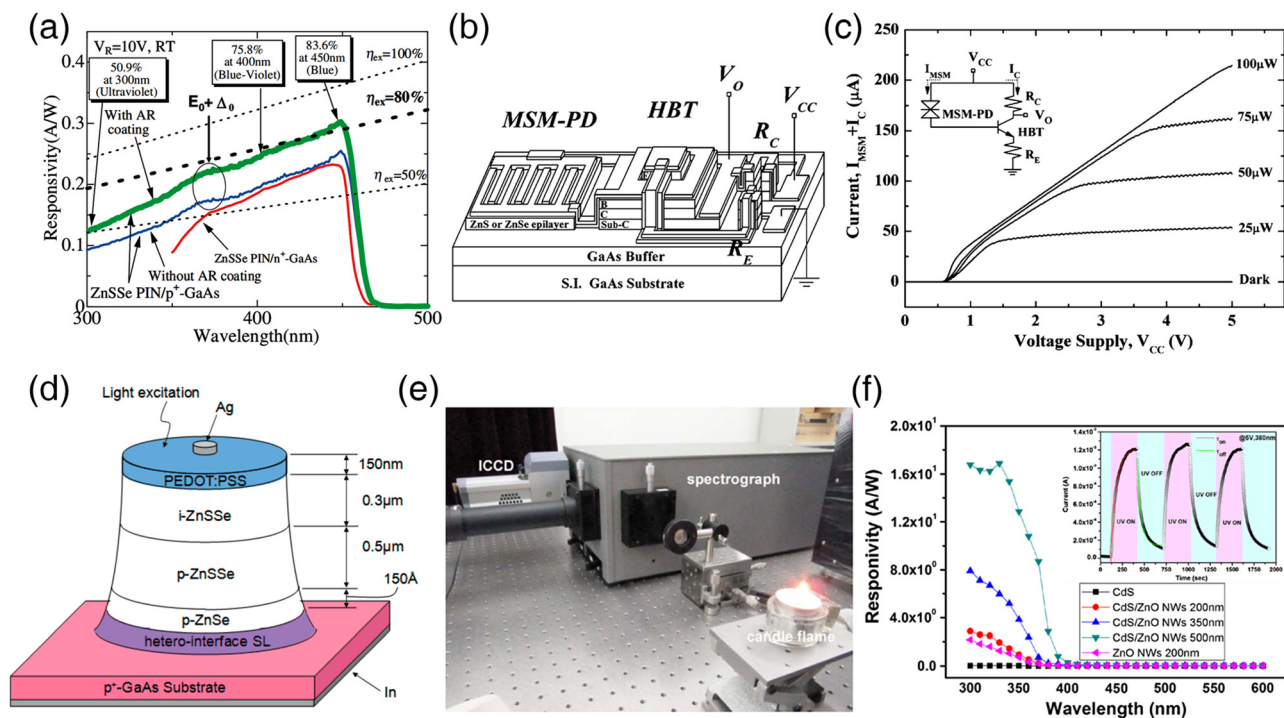


Fig. 8 (a) Spectral sensitivities of the n^+ -i-p structure ZnSe PIN on p^+ -GaAs. Reproduced with permission from ref. 116. Copyright 2006, John Wiley and Sons. (b) Schematic cross-sectional diagram of the fabricated integrated photodetector. (c) I - V characteristics of the ZnSe-based integrated photodetector, and the inset shows the circuit diagram designed for the device. Reproduced with permission from ref. 117. Copyright 2009, IOP Publishing. (d) Schematic structures of organic-inorganic hybrid photodetectors. Reproduced with permission from ref. 118. Copyright 2010, John Wiley and Sons. (e) Experimental setup for capturing emission spectra from the candle flame. Reproduced with permission from ref. 119. Copyright 2011, IEEE. (f) Photoresponsivity of the various length ZnO NW/CdS devices as a function of the illumination wavelength. Inset: I - t curves of the length ZnO (500 nm) on the CdS photodetector. Reproduced with permission from ref. 120. Copyright 2017, Springer Nature.

3.3 Other structured materials for photodetectors

Besides the above semiconductor nanostructures, some solid-state thin films are also good candidates for constructing high-performance UVPDs. In the past few decades, various sophisticated techniques, such as MOCVD, MBE, PLD, and some solution synthesis methods, have been developing rapidly, which have provided vast opportunities for thin-film materials.^{25,113–115} Wong *et al.* developed an autocorrelator based on two-photon absorption of ZnSSe photodetectors for the first time.¹¹³ This autocorrelator is capable of measuring femtosecond laser pulses ranging from 800 to 400 nm and has the advantages of a broad bandwidth, high sensitivity, and high repetition rate. Miki *et al.* demonstrated the UV PIN photodiodes based on the ZnSSe n⁺-i-p structure/p⁺-GaAs substrate.¹¹⁶ Due to the ultra-thin n⁺ window layer (~ 200 Å) and a high-energy valence band effect, the responsivity of the ZnSSe n⁺-i-p/p⁺-GaAs photodetector in the UV region is drastically improved compared with the ZnSSe PIN/n⁺-GaAs device (Fig. 8a). Chen *et al.* successfully fabricated monolithically integrated photodetectors composed of a heterojunction bipolar transistor (HBT) and a ZnS and ZnSe metal–semiconductor–metal (MSM) photodiode using a patterned oxide growth technique (Fig. 8b).¹¹⁷ In this work, the ZnS and ZnSe MSM photodiodes showed responsivities of 0.028 and 0.08 A W⁻¹, respectively. Moreover, the ZnS ($R_{320\text{ nm}}/R_{485\text{ nm}}$) and ZnSe ($R_{440\text{ nm}}/R_{600\text{ nm}}$) devices exhibited high rejection ratios of

2.6×10^3 and 1.6×10^3 , respectively. The voltage amplification sensitivities were $-8.7\text{ mV } \mu\text{W}^{-1}$ and $-29.6\text{ mV } \mu\text{W}^{-1}$ for the ZnS- and ZnSe-based integrated photodetectors, respectively. As shown in Fig. 8c, the knee voltage depends on the intensity of the optical input power, and the required voltage supply for the device increases with the input optical power intensity. The maximal measurable input optical power intensities were 273 and 94 μW , respectively. In 2010, organic–inorganic hybrid Schottky-type photodetectors with the conducting polymer as a window layer on ZnSSe/p-GaAs wafers have been demonstrated (Fig. 8d).¹¹⁸ The present device exhibited a high EQE of 80% (300 nm) in the UV region, which is higher than that of the commercial Si UV photodiode (54%). Furthermore, this device also shows a high EQE in the DUV region (71% at 250 nm). Meanwhile, the dark current density of the photodiode is as low as 10 pA mm⁻² at a reverse bias of 10 V. Cheong *et al.* developed a ZigBee-based wireless sensor network node for the UV detection of flames.¹¹⁹ In this device, the ZnSSe-alloy was deposited on an epi-ready 2-in device wafer on n⁺-GaAs(100) substrates by the MBE technique. The sensor node consists of a ZnSSe UVPD, a current-sensitive front-end, and other components. The experimental setup is shown in Fig. 8e. The sensor node has a reliable flame detection speed of 70 ms and consumes an average of only 2.3 mW at a bias of 3.3 V. In addition, the high surface-to-volume ratio of nanostructures has

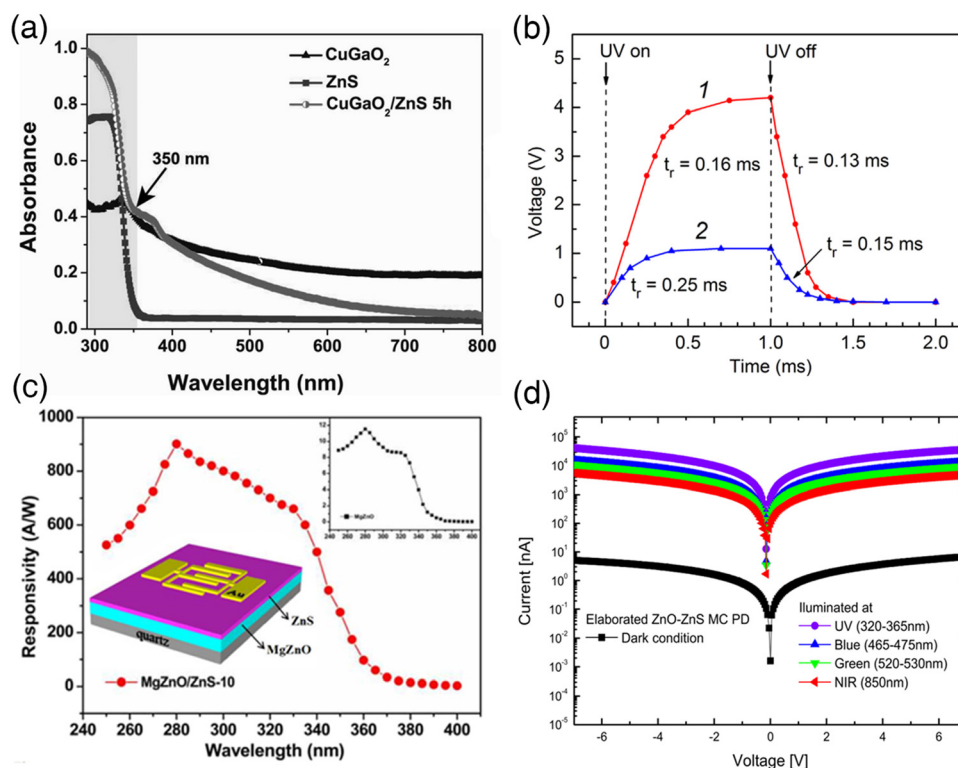


Fig. 9 (a) UV-vis absorption spectra of CuGaO₂, ZnS films, and CuGaO₂/ZnS heterostructured thin films on the quartz glass. Reproduced with permission from ref. 121. Copyright 2017, John Wiley and Sons. (b) *I*-*t* characteristics of ZnSe-based MSM UVPDs under a 325 nm Cd–He laser illumination. Reproduced with permission from ref. 57. Copyright 2017, John Wiley and Sons. (c) The responsivity of the MgZnO/ZnS device. Inset: Structure of the MSM MgZnO/ZnS heterojunction UVPD. Reproduced with permission from ref. 52. Copyright 2020, Elsevier. (d) *I*-*V* characteristics in the logarithmic scale of the UV-vis-NIR photodetector based on the ZnO–ZnS microstructured composite. Reproduced with permission from ref. 124. Copyright 2021, Elsevier.

an important contribution to improve the carrier collection efficiency of the device. The UVPDs with ZnO nanorods/CdS thin film heterostructures have been fabricated by Lam *et al.* in 2017.¹²⁰ The UV photoresponsivity of the device becomes higher as the ZnO nanorod length was increased (Fig. 8f), attributed to the high surface-to-volume ratio of the ZnO nanostructure easily providing a carrier collection efficiency.

On the other hand, heterojunctions made of ZnS and other semiconductor materials also find promising applications in the assembly of sensitive UVPDs. By using a simple strategy associated with the oil/water interfacial self-assembly approach, Li *et al.* synthesized the large-area CuGaO₂/ZnS heterojunctions by growing ZnS microspheres on the top surface of CuGaO₂ hexagonal platelets.¹²¹ As shown in Fig. 9a, the UV light adsorption of CuGaO₂/ZnS heterostructured thin film is apparently higher than that of the unitary ZnS microsphere films. The UVPD based on CuGaO₂/ZnS heterostructured films shows a low dark current of 35.2 pA at 5.0 V. Xu *et al.* fabricated the transparent diodes based on p-type CuS-ZnS/n-type ZnO thin

films by sequential chemical bath and sol-gel spin methods.⁵⁹ This UVPD shows a self-powered characteristic, and has a fast photoresponse under an UV light illumination of 300 nm. In 2018, Liu *et al.* developed a compact solid-state UV flame sensing system based on a wide bandgap II-VI group thin film semiconductor.¹²² The MBE-grown Cr/ZnSSe Schottky barrier UVPD is used as the UV light sensing element. In this sensing system, the average gain of the amplification circuit is 16 600, and the feedback resistance is 50 GΩ. The overall photoresponse of the developed flame sensing system displays a maximum spectral response at 250 nm with a long-wavelength rejection power of approximately ten orders. In addition, the system avoids the effect of indoor lighting on the detection results. This sensing system has a good detection effect on the butane flame within 10 cm, suggesting that it has great potential in fire safety applications.

For the ZnSe crystal based MSM photodetector without interdigital contacts, the device shows a high rejection ratio of 7900 and a low dark current (3.4 nA).⁵⁷ As shown in Fig. 9b,

Table 2 Summary of the performance parameters of some representative UVPDs based on II-VI group semiconductors

Device geometries	Mode	λ [nm]	I_{dark} [nA]	R [A W ⁻¹]	D^* [Jones]	τ_r [s]/ τ_d [s]	Ref.
ZnS nanoribbons	Photoconductor	254	—	2.9×10^6	—	76/463	43
ZnS/ZnO microspheres	Photoconductor	350	15.1	94.5	—	—	98
ZnS/ZnO nanobelts	Photoconductor	320	3030	5×10^5	—	0.3/1.5	44
ZnS QDs	Photoconductor	254	0.27	1.6×10^{-3}	5.51×10^9	1.1	45
ZnS nanowires	Phototransistor	254	—	4.7×10^6	—	95/209	63
ZnS: Ga nanoribbons	Photoconductor	320	—	5×10^5	1.3×10^{19}	0.0032/0.01	46
ZnS/SnO ₂ nanoribbons	Heterostructure	320	3500	6.2×10^4	—	8/61	58
ZnO/ZnSe nanowires	Heterostructure	385	2.77×10^5	8.7	—	—	125
ZnS nanorods	Photoconductor	340	—	0.056	—	0.04	47
ZnS/CdS nanobelts	Heterostructure	450	10^{-3}	—	2.23×10^{14}	0.005/0007	107
Gr/ZnS film	Phototransistor	365	2.79×10^{-6}	1.7×10^7	—	0.05/3.5	64
p-CuZnS/n-ZnO films	Heterostructure	300	—	0.012	—	0.7/0.86	59
Gr/ZnSe film	Phototransistor	365	2.43×10^{-6}	3.9×10^6	—	0.03/0.04	64
ZnS nanotubes	Photoconductor	Xenon lamp	8.44×10^{-3}	16.5	1.41×10^9	0.12/0.4	48
ZnS nanowires	Photoconductor	254	—	4.97×10^6	—	9/24	49
ZnS/InP nanowires	Heterostructure	332	—	295	1.65×10^{13}	0.75/0.5	60
ZnS nanotubes	Photoconductor	Xenon lamp	0.015	2.56	1.67×10^{10}	0.09/0.07	50
ZnS QDs	Heterostructure	320	—	0.19	—	0.024/0.011	61
ZnO/ZnS nanorods	Heterostructure	370	0.74	0.104	—	—	126
ZnS film	Photoconductor	350	1.04	4970	—	0.05/1.03	51
ZnSe/ZnS QDs	Phototransistor	405	—	2000	—	0.52	62
Gr/ZnS QDs/4H-SiC	Heterostructure	250	55.64	2.9×10^{-4}	1.41×10^{10}	2.8×10^{-7}	23
ZnS QDs	Photoconductor	365	—	5.8	1.97×10^{13}	—	127
ZnS/MgZnO film	Heterostructure	325	1	900	9×10^{14}	4.12/3.26	52
ZnS: Mn nanorods	Photoconductor	310	—	1.62	—	10^{-3}	112
ZnS microspheres	Photoconductor	365	—	2.74×10^{-4}	2.02×10^9	0.15/0.21	53
ZnS nanobelts	Photoconductor	365	—	1.8×10^3	3.3×10^{13}	0.04/0.05	54
ZnS: Mn ²⁺ QDs	Photoconductor	255	500	0.2	1.2×10^{11}	6.5×10^{-7}	55
ZnO/ZnS nanowires	Heterostructure	385	1.2×10^4	0.2	—	—	106
ZnS/ZnO nanobelts	Photoconductor	320	670	5×10^5	—	0.3/1.7	44
ZnSe film	Photoconductor	448	—	0.128	2.44×10^{11}	—	114
ZnSe-nanobelts	Photoconductor	400	10^{-5}	0.12	—	0.3	19
ZnSe: Cl nanoribbons	Photoconductor	460	—	7.9×10^5	—	0.3	56
ZnO/ZnSe nanowires	Heterostructure	385	10^5	27.1	—	—	125
ZnSe crystal	Photoconductor	325	3.4	4.44	1.4×10^{11}	1.6×10^{-4}	57
ZnSSe film	Photoconductor	330	10^{-4}	0.163	1.28×10^{13}	—	115
ZnSSe/GaAs	PIN photodiode	300	10^{-3}	0.12	—	—	116
ZnSSe/p-GaAs	Schottky diode	300	0.01	0.2	—	—	118
ZnSSe/ZnSe nanowires	Heterostructure	360	10^{-3}	6.3×10^5	—	10^{-4}	10
ZnCdS/ZnMgS/GaP films	Heterostructure	320	10^{-3}	0.11	—	—	128
ZnCdS/ZnS/GaP films	Photoconductor	350	10^{-4}	0.03	—	—	129
ZnSSe films	Photodiode	400	0.58	0.19	—	—	25

the rise and decay time were estimated to be 0.25 and 0.15 ms, respectively, for the photodetector without interdigital electrodes (Fig. 9b). In addition, a broadband flat panel photodetector integrated a ZnS photoconductor and ZnO nanowire field emitters and exhibits a high R of $5.93 \times 10^2 \text{ A W}^{-1}$ and an EQE of $1.03 \times 10^5\%$ under 350 nm light.⁵¹ The effect of a ZnSe/ZnS/GaAs distributed Bragg reflector on the spectral response of an MSM-diode was investigated by Averin *et al.* in 2020.¹²³ The experimental results showed that the MSM photodiode was based on a periodic ZnSe/ZnS/GaAs heterostructure from a distributed Bragg reflector. This detector shows a low dark current of $5 \times 10^{-10} \text{ A}$ at 40 V, and the response wavelength of the photodetector can be adjusted by appropriately selecting the parameters of the heterostructure layers. The MgZnO/ZnS heterojunction-based UVPD also exhibits excellent performance.⁵² Compared with the MgZnO photodetector, the MgZnO/ZnS heterojunction-based UVPD has a low dark current of 1 nA and an ultrahigh photo-to-dark current ratio (up to 10^5). Moreover, this heterojunction device also exhibits a remarkable responsivity of 900 A W^{-1} (Fig. 9c). In 2021, Benyahia *et al.* demonstrated a broadband multispectral photodetector that exhibited a high UV-vis-NIR photoresponse.¹²⁴ Furthermore, the sensitive device composed of ZnO/ZnS heterostructures also achieves an apparent photovoltaic effect with UV, visible and NIR photocurrent values of 0.7, 0.2 and 0.1 μA at $V = 0 \text{ V}$, respectively (Fig. 9d).

The above study has shown that low-dimensional II–VI group semiconductor nanostructures (*e.g.*, 0D, 1D and 2D) are promising building blocks for the assembly of various sensitive UVPDs. The detection range of these devices is determined by not only the size of the QDs or nanoparticles, but also the bandgap of other II–VI group semiconductors. Some UVPDs based on 1D II–VI group semiconductors exhibit an ultra-high photoresponsivity ($> 10^5 \text{ A W}^{-1}$), such as nanoribbons, nanobelts, and nanowires.^{10,43,44,49,63} After optimizing the device structure, the photodetectors often show a faster response speed.^{10,23,46,57,107} We summarize the important parameters of UVPDs based on various types of II–VI group semiconductor nanostructures in Table 2.

4. Conclusion and outlooks

II–VI group semiconductors prove to be the promising materials (nanostructures, thin films, single crystals, *etc.*) in assembling high-performance UVPDs. In this review article, we summarize the basic concepts and evaluation parameters of the UVPDs, and then the research progress and the applications of UVPDs based on II–VI group semiconductors are briefly reviewed. Due to the small device size, photodetectors based on ZnS and ZnSe nanostructures exhibit a high responsivity and fast response speed. Besides, on the basis of the quantum confinement effect, the bandgap can be increased by reducing the size of II–VI group semiconductor quantum dots, thereby the detection band of the device can be further broadened. Considering the continuous development of the semiconductor process and integrated circuit technology, the performance of UVPDs is likely to improve

in the future. Furthermore, II–VI group semiconductor UVPDs have been initially used in image sensing, flame detection, *etc.* Despite the great progress obtained in the research of UVPDs based on II–VI group semiconductors, the realization of high-performance devices and their large-scale applications still faces many challenges:

(1) High responsivity and fast response speed are difficult to achieve simultaneously. The photoconductor has a slow response speed because of the persistent photoconductivity (PPC) effect. Photodetectors based on the photovoltaic effect usually have a faster response speed owing to the built-in electric field, but the device responsivity is low due to the short carrier lifetime. Therefore, there is a trade-off between the responsivity and response speed. To overcome this challenge, 2D materials may be used as the active layer of the device, and the light absorption can be increased by improving the device structure. This will improve the photoresponsivity while maintaining a relatively short carrier lifetime.

(2) It is a significant challenge to fabricate large-scale and high-performance integrated systems for UVPDs. Among the research achievements, the II–VI group semiconductor UVPDs have been applied in flame detection, image sensing and other fields. However, in flame detection, the detection distance is still short and has low sensitivity. The image sensing system has some deficiencies, such as the low resolution and single colour. In the following work, we should combine the circuit design principles to develop the relevant device integration technology, develop large-area array detection with a low power consumption, small size, high sensitivity and high integration and study the weak signal processing technology. These will pave the way for II–VI group semiconductor UVPDs in becoming an essential part of future commercial electronic and optoelectronic components.

Conflicts of interest

The authors declare no conflicts of interest.

Acknowledgements

This work was supported by the National Natural Science Foundation of China (NSFC, No. 62074048 and 61675062), the Key Research and Development Plan of Anhui Province (2022f04020007), and the Fundamental Research Funds for the Central Universities (PA2020GDKC0014 and JZ2018HGXC0001).

References

- 1 E. Munoz, E. Monroy, J. Pau, F. Calle, F. Omnes and P. Gibart, *J. Phys.: Condens. Matter*, 2001, **13**, 7115–7137.
- 2 L. Sang, M. Liao and M. Sumiya, *Sensors*, 2013, **13**, 10482–10518.
- 3 H. Chen, K. Liu, L. Hu, A. A. Al-Ghamdi and X. Fang, *Mater. Today*, 2015, **18**, 493–502.

- 4 D. Guo, H. Liu, P. Li, Z. Wu, S. Wang, C. Cui, C. Li and W. Tang, *ACS Appl. Mater. Interfaces*, 2017, **9**, 1619–1628.
- 5 W. Y. Weng, T. J. Hsueh, S. J. Chang, G. J. Huang and H. T. Hsueh, *IEEE Photonics Technol. Lett.*, 2011, **23**, 444–446.
- 6 C. Xie, X.-T. Lu, X.-W. Tong, Z.-X. Zhang, F.-X. Liang, L. Liang, L.-B. Luo and Y.-C. Wu, *Adv. Funct. Mater.*, 2019, **29**, 1806006.
- 7 F. Zhang, S. Niu, W. Guo, G. Zhu, Y. Liu, X. Zhang and Z. L. Wang, *ACS Nano*, 2013, **7**, 4537–4544.
- 8 J. Kim, H. Hiroi, T. K. Todorov, O. Gunawan, M. Kuwahara, T. Gokmen, D. Nair, M. Hopstaken, B. Shin, Y. S. Lee, W. Wang, H. Sugimoto and D. B. Mitzi, *Adv. Mater.*, 2014, **26**, 7427–7431.
- 9 X. Xu, S. Li, J. Chen, S. Cai, Z. Long and X. Fang, *Adv. Funct. Mater.*, 2018, **28**, 1802029.
- 10 Z. Mu, Q. Zheng, R. Liu, M. W. I. Malik, D. Tang, W. Zhou and Q. Wan, *Adv. Electron. Mater.*, 2019, **5**, 1800770.
- 11 M. N. Yoder, *IEEE Trans. Electron Devices*, 1996, **43**, 1633–1636.
- 12 M. Que, C. Lin, J. Sun, L. Chen, X. Sun and Y. Sun, *Sensors*, 2021, **21**, 5502.
- 13 J.-L. Yang, K.-W. Liu and D.-Z. Shen, *Chin. Phys. B*, 2017, **26**, 047308.
- 14 K. Liu, M. Sakurai and M. Aono, *Sensors*, 2010, **10**, 8604–8634.
- 15 B. Deka Boruah, *Nanoscale Adv.*, 2019, **1**, 2059–2085.
- 16 L. Qin, F. J. Mawignon, M. Hussain, N. K. Ange, S. Lu, M. Hafezi and G. Dong, *Materials*, 2021, **14**, 4083.
- 17 L. Wang, M. Lu, L. V. Peng, J. Jie, T. Yan, Y. Yu, C. Wu, Y. Zhang, C. Xie, P. Jiang, Z. Wang and Z. Hu, *Sci. Adv. Mater.*, 2012, **4**, 332–336.
- 18 Y. Liang, H. Liang, X. Xiao and S. Hark, *J. Mater. Chem.*, 2012, **22**, 1199–1205.
- 19 X. Fang, S. Xiong, T. Zhai, Y. Bando, M. Liao, U. K. Gautam, Y. Koide, X. Zhang, Y. Qian and D. Golberg, *Adv. Mater.*, 2009, **21**, 5016–5021.
- 20 B. Nie, L. B. Luo, J. J. Chen, J. G. Hu, C. Y. Wu, L. Wang, Y. Q. Yu, Z. F. Zhu and J. S. Jie, *Nanotechnology*, 2013, **24**, 095603.
- 21 D. Wu, Y. Jiang, Y. Yu, Y. Zhang, G. Li, Z. Zhu, C. Wu, L. Wang, L. Luo and J. Jie, *Nanotechnology*, 2012, **23**, 485203.
- 22 T.-Y. Wei, C.-T. Huang, B. J. Hansen, Y.-F. Lin, L.-J. Chen, S.-Y. Lu and Z. L. Wang, *Appl. Phys. Lett.*, 2010, **96**, 013508.
- 23 H. Kan, W. Zheng, R. Lin, M. Li, C. Fu, H. Sun, M. Dong, C. Xu, J. Luo, Y. Fu and F. Huang, *ACS Appl. Mater. Interfaces*, 2019, **11**, 8412–8418.
- 24 Y. Yuan, Y. Han, B. Huang, L. Zhang, H. Yang, B. Gu, Y. Cui and J. Zhang, *Nanotechnology*, 2019, **30**, 075501.
- 25 L. S. Lai, I. K. Sou, C. W. Y. Law, K. S. Wong, Z. Yang and G. K. L. Wong, *Opt. Mater.*, 2003, **23**, 21–26.
- 26 P. T. Gomathi, P. Sahatiya and S. Badhulika, *Adv. Funct. Mater.*, 2017, **27**, 1701611.
- 27 X.-X. Yu, H. Yin, H.-X. Li, H. Zhao, C. Li and M.-Q. Zhu, *J. Mater. Chem. C*, 2018, **6**, 630–636.
- 28 D. L. Rode, *Phys. Rev. B: Solid State*, 1970, **2**, 4036–4044.
- 29 G. A. Samara, *Phys. Rev. B: Condens. Matter Mater. Phys.*, 1983, **27**, 3494–3505.
- 30 S. Ebrahimi, B. Yarmand and N. Naderi, *Thin Solid Films*, 2019, **676**, 31–41.
- 31 N. A. Al-Tememe, N. M. Saeed, S. M. A. Al-Dujayli and B. T. Chiad, *Adv. Mater. Phys. Chem.*, 2012, **02**, 69–74.
- 32 A. Dinger, S. Petillon, M. Grün, M. Hetterich and C. Klingshirn, *Semicond. Sci. Technol.*, 1999, **14**, 595–598.
- 33 S. Bratskaya, K. Sergeeva, M. Konovalova, E. Modin, E. Svirshchevskaya, A. Sergeev, A. Mironenko and A. Pestov, *Colloids Surf., B*, 2019, **182**, 110342.
- 34 Y. Zhang, J. Wei, T. Liu, Z. Zhong, Z. Luo, W. Xiao, B. Lv, X. Zhou and X. Liu, *Appl. Surf. Sci.*, 2022, **574**, 151679.
- 35 W. Leigh and B. W. Wessels, *Appl. Phys. Lett.*, 1982, **41**, 165–167.
- 36 V. Kumar, M. K. Sharma, G. S. Sandhu, S. Sharmac and T. P. Sharm, 2007 *International Workshop on Physics of Semiconductor Devices*, IEEE, 2007, pp. 483–486.
- 37 D. Merbach, E. Schöll, W. Ebeling, P. Michler and J. Gutowski, *Phys. Rev. B: Condens. Matter Mater. Phys.*, 1998, **58**, 10709–10720.
- 38 M. J. Kastner, B. Hahn, C. Auchter, M. Deufel, A. Rosenauer and W. Gebhardt, *J. Cryst. Growth*, 1996, **159**, 134–137.
- 39 T. A. Chynoweth and R. H. Bube, *J. Appl. Phys.*, 1980, **51**, 1844–1846.
- 40 P. J. Wright, B. Cockayne and A. J. Williams, *J. Cryst. Growth*, 1985, **72**, 23–26.
- 41 M. A. Rafea, A. A. M. Farag and N. Roushdy, *J. Alloys Compd.*, 2009, **485**, 660–666.
- 42 J. Datta, M. Das, A. Dey, S. Halder, S. Sil and P. P. Ray, *Appl. Surf. Sci.*, 2017, **420**, 566–578.
- 43 Y. Yu, J. Jie, P. Jiang, L. Wang, C. Wu, Q. Peng, X. Zhang, Z. Wang, C. Xie, D. Wu and Y. Jiang, *J. Mater. Chem.*, 2011, **21**, 12632–12638.
- 44 L. Hu, J. Yan, M. Liao, H. Xiang, X. Gong, L. Zhang and X. Fang, *Adv. Mater.*, 2012, **24**, 2305–2309.
- 45 W.-J. Kuang, X. Liu, Q. Li, Y.-Z. Liu, J. Su and H. Tolner, *IEEE Photonics Technol. Lett.*, 2018, **30**, 1384–1387.
- 46 Y. Yu, Y. Jiang, K. Zheng, Z. Zhu, X. Lan, Y. Zhang, Y. Zhang and X. Xuan, *J. Mater. Chem. C*, 2014, **2**, 3583–3588.
- 47 H. Lin, L. Wei, C. Wu, Y. Chen, S. Yan, L. Mei and J. Jiao, *Nanoscale Res. Lett.*, 2016, **11**, 1–7.
- 48 Q. An, X. Meng, K. Xiong, Y. Qiu and W. Lin, *Nanotechnology*, 2017, **28**, 105502.
- 49 S. H. Yen, Y. C. Hung, P. H. Yeh, Y. W. Su and C. Y. Wang, *Nanotechnology*, 2017, **28**, 395201.
- 50 Q. An, X. Meng, K. Xiong and Y. Qiu, *Sci. Rep.*, 2017, **7**, 1–12.
- 51 Z. Zhang, K. Wang, K. Zheng, S. Deng, N. Xu and J. Chen, *J. Lightwave Technol.*, 2018, **36**, 5010–5015.
- 52 Y. Zhu, Y. Zhang, L. Yan, D. Zhang, J. Zhou, S. Adimi and S. Ruan, *J. Alloys Compd.*, 2020, **832**, 155022.
- 53 A. Kumar, M. Kumar, V. Bhatt, D. Kim, S. Mukherjee, J.-H. Yun and R. K. Choubey, *Chem. Phys. Lett.*, 2021, **763**, 138162.
- 54 G. Wang and X. Meng, *Mater. Lett.*, 2022, **309**, 131306.
- 55 K. Gogoi and A. Chattopadhyay, *Langmuir*, 2022, **38**, 2668–2676.

- 56 Z. Wang, J. Jie, F. Li, L. Wang, T. Yan, L. Luo, B. Nie, C. Xie, P. Jiang, X. Zhang, Y. Yu and C. Wu, *ChemPlusChem*, 2012, **77**, 470–475.
- 57 V. P. Sirkeli, O. Yilmazoglu, A. S. Hajo, N. D. Nedeoglo, D. D. Nedeoglo, S. Preu, F. Küppers and H. L. Hartnagel, *Phys. Status Solidi RRL*, 2018, **12**, 1700418.
- 58 X. Huang, Y. Q. Yu, J. Xia, H. Fan, L. Wang, M. G. Willinger, X. P. Yang, Y. Jiang, T. R. Zhang and X. M. Meng, *Nanoscale*, 2015, **7**, 5311–5319.
- 59 X. Xu, S. Shukla, Y. Liu, B. Yue, J. Bullock, L. Su, Y. Li, A. Javey, X. Fang and J. W. Ager, *Phys. Status Solidi RRL*, 2017, **12**, 1700381.
- 60 K. Zhang, J. Ding, Z. Lou, R. Chai, M. Zhong and G. Shen, *Nanoscale*, 2017, **9**, 15416–15422.
- 61 R. Xu, S. Ruan, D. Zhang, Z. Li, B. Yin, K. Li, J. Zhou, Y. Chen and C. Li, *J. Alloys Compd.*, 2018, **751**, 117–123.
- 62 Y. L. Sun, D. Xie, M. X. Sun, C. J. Teng, L. Qian, R. S. Chen, L. Xiang and T. L. Ren, *Sci. Rep.*, 2018, **8**, 5107.
- 63 P. Jiang, J. Jie, Y. Yu, Z. Wang, C. Xie, X. Zhang, C. Wu, L. Wang, Z. Zhu and L. Luo, *J. Mater. Chem.*, 2012, **22**, 6856–6861.
- 64 F. Huang, F. Jia, C. Cai, Z. Xu, C. Wu, Y. Ma, G. Fei and M. Wang, *Sci. Rep.*, 2016, **6**, 28943.
- 65 Y. Peng, Y. Zhang, Z. Chen, D. Guo, X. Zhang, P. Li, Z. Wu and W. Tang, *IEEE Photonics Technol. Lett.*, 2018, **30**, 993–996.
- 66 G. Konstantatos and E. H. Sargent, *Nat. Nanotechnol.*, 2010, **5**, 391–400.
- 67 A. Rose, *Concepts in Photoconductivity and Allied Problems*, Interscience Publishers, New York, 1963.
- 68 E. Monroy, F. Omnès and F. Calle, *Semicond. Sci. Technol.*, 2003, **18**, R33.
- 69 Y. Xu and Q. Lin, *Appl. Phys. Rev.*, 2020, **7**, 011315.
- 70 D. K. Karan, P. Panda and G. N. Dash, *J. Semicond.*, 2013, **34**, 014001.
- 71 P. Dutta and P. M. Horn, *Rev. Mod. Phys.*, 1981, **53**, 497–516.
- 72 F. H. Koppens, T. Mueller, P. Avouris, A. C. Ferrari, M. S. Vitiello and M. Polini, *Nat. Nanotechnol.*, 2014, **9**, 780–793.
- 73 X. Gong, M. Tong, Y. Xia, W. Cai, J. S. Moon, Y. Cao, G. Yu, C. L. Shieh, B. Nilsson and A. J. Heeger, *Science*, 2009, **325**, 1665–1667.
- 74 Y. Fang, A. Armin, P. Meredith and J. Huang, *Nat. Photonics*, 2018, **13**, 1–4.
- 75 D. Kaur and M. Kumar, *Adv. Opt. Mater.*, 2021, **9**, 2002160.
- 76 P. Feng, I. Mönch, S. Harazim, G. Huang, Y. Mei and O. G. Schmidt, *Nano Lett.*, 2009, **9**, 3453–3459.
- 77 K. Liu, M. Sakurai, M. Aono and D. Shen, *Adv. Funct. Mater.*, 2015, **25**, 3157–3163.
- 78 C. H. Qiu and J. I. Pankove, *Appl. Phys. Lett.*, 1997, **70**, 1983–1985.
- 79 H. M. Chen, Y. F. Chen, M. C. Lee and M. S. Feng, *J. Appl. Phys.*, 1997, **82**, 899–901.
- 80 J. Chen, W. Ouyang, W. Yang, J. H. He and X. Fang, *Adv. Funct. Mater.*, 2020, **30**, 1909909.
- 81 L. Wang, X. Ma, R. Chen, Y.-Q. Yu and L.-B. Luo, *J. Mater. Sci.: Mater. Electron.*, 2015, **26**, 4290–4297.
- 82 F. P. García de Arquer, A. Armin, P. Meredith and E. H. Sargent, *Nat. Rev. Mater.*, 2017, **2**, 1–17.
- 83 Q. Peng, J. Jie, C. Xie, L. Wang, X. Zhang, D. Wu, Y. Yu, C. Wu, Z. Wang and P. Jiang, *Appl. Phys. Lett.*, 2011, **98**, 123117.
- 84 J. Zhang and W. R. Harrell, *J. Vac. Sci. Technol., B*, 2003, **21**, 872–878.
- 85 L. Dai, J. Liu, C. Han, Z. Wang, Y. Zhang and Z. Hu, *Phys. Status Solidi A*, 2015, **212**, 2791–2797.
- 86 C. R. Crowell and S. M. Sze, *Solid-State Electron.*, 1966, **9**, 1035–1048.
- 87 L. Wang, M. Lu, X. Wang, Y. Yu, X. Zhao, P. Lv, H. Song, X. Zhang, L. Luo, C. Wu, Y. Zhang and J. Jie, *J. Mater. Chem. A*, 2013, **1**, 1148–1154.
- 88 C. Y. Wu, *J. Appl. Phys.*, 1982, **53**, 5947–5950.
- 89 Y. Yang, W. Guo, J. Qi, J. Zhao and Y. Zhang, *Appl. Phys. Lett.*, 2010, **97**, 223113.
- 90 A. M. Strel'chuk, V. S. Kiselev and S. F. Avramenko, *Mater. Sci. Eng. B*, 1999, **61–62**, 437–440.
- 91 R. O'Hayre, M. Nanu, J. Schoonman and A. Goossens, *J. Phys. Chem. C*, 2007, **111**, 4809–4814.
- 92 D. Mao, J. Peng, Z. Xin, Y. Tian, J. Wu, S. Hu, Y. Lv, S. Tian and Y. Ling, *J. Appl. Phys.*, 2020, **128**, 124503.
- 93 A. Muhammetgulyyev, O. G. Erbas, B. Kinaci, O. Donmez, Y. G. Celebi and A. Erol, *Semicond. Sci. Technol.*, 2019, **34**, 085001.
- 94 L. B. Luo, W. J. Xie, Y. F. Zou, Y. Q. Yu, F. X. Liang, Z. J. Huang and K. Y. Zhou, *Opt. Express*, 2015, **23**, 12979–12988.
- 95 O. Katz, V. Garber, B. Meyler, G. Bahir and J. Salzman, *Appl. Phys. Lett.*, 2001, **79**, 1417–1419.
- 96 X. Chen, F. Ren, S. Gu and J. Ye, *Photonics Res.*, 2019, **7**, 381–415.
- 97 O. Katz, G. Bahir and J. Salzman, *Appl. Phys. Lett.*, 2004, **84**, 4092–4094.
- 98 L. Hu, M. Chen, W. Shan, T. Zhan, M. Liao, X. Fang, X. Hu and L. Wu, *Adv. Mater.*, 2012, **24**, 5872–5877.
- 99 D. Spirito, S. Kudera, V. Miseikis, C. Giansante, C. Coletti and R. Krahne, *J. Phys. Chem. C*, 2015, **119**, 23859–23864.
- 100 R. Saran and R. J. Curry, *Nat. Photonics*, 2016, **10**, 81–92.
- 101 Sunaina, A. K. Ganguli and S. K. Mehta, *J. Alloys Compd.*, 2022, **894**, 162263.
- 102 Y. Liu, C. Zhao, J. Li, S. Zhao, X. Xu, H. Y. Fu, C. Yu, F. Kang and G. Wei, *ACS Appl. Electron. Mater.*, 2021, **3**, 1236–1243.
- 103 W.-J. Kuang, Z.-P. Wang, H. Liu, Y.-F. Ding, Q.-M. Xu, R.-H. Guo, Q. Li and H. Tolner, *IEEE Photonics Technol. Lett.*, 2020, **32**, 204–207.
- 104 X. Fang, Y. Bando, M. Liao, T. Zhai, U. K. Gautam, L. Li, Y. Koide and D. Golberg, *Adv. Funct. Mater.*, 2010, **20**, 500–508.
- 105 W. Tian, C. Zhang, T. Zhai, S. L. Li, X. Wang, J. Liu, X. Jie, D. Liu, M. Liao, Y. Koide, D. Golberg and Y. Bando, *Adv. Mater.*, 2014, **26**, 3088–3093.
- 106 S. C. Rai, K. Wang, Y. Ding, J. K. Marmon, M. Bhatt, Y. Zhang, W. Zhou and Z. L. Wang, *ACS Nano*, 2015, **9**, 6419–6427.

- 107 Z. Lou, L. Li and G. Shen, *Nanoscale*, 2016, **8**, 5219–5225.
- 108 D. Zheng, H. Fang, P. Wang, W. Luo, F. Gong, J. C. Ho, X. Chen, W. Lu, L. Liao, J. Wang and W. Hu, *Adv. Funct. Mater.*, 2016, **26**, 7690–7696.
- 109 C. Wu, F. Wang, C. Cai, Z. Xu, Y. Ma, F. Huang, F. Jia and M. Wang, *2D Mater.*, 2017, **4**, 025113.
- 110 Z. Xu, C. Wu, A. Li, Y. Ma, G. T. Fei and M. Wang, *IEEE Electron Device Lett.*, 2018, **39**, 240–243.
- 111 X. Li, S. Gao, G. Wang, Z. Xu, S. Jiao, D. Wang, Y. Huang, D. Sang, J. Wang and Y. Zhang, *J. Mater. Chem. C*, 2020, **8**, 1353–1358.
- 112 S. Saeed, R. Dai, R. A. Janjua, D. Huang, H. Wang, Z. Wang, Z. Ding and Z. Zhang, *ACS Omega*, 2021, **6**, 32930–32937.
- 113 K. S. Wong, T. Sun, B. K. K. Fung, I. K. Sou and G. K. L. Wong, *J. Cryst. Growth*, 2001, **227–228**, 717–721.
- 114 T. K. Lin, S. J. Chang, Y. K. Su, Y. Z. Chiou, C. K. Wang, S. P. Chang, C. M. Chang, J. J. Tang and B. R. Huang, *Mater. Sci. Eng. B*, 2005, **119**, 202–205.
- 115 L. S. Mak, S. K. Chan, G. K. L. Wong and I. K. Sou, *J. Electron. Mater.*, 2006, **35**, 1322–1326.
- 116 K. Miki, T. Abe, J. Naruse, K. Ikumi, T. Yamaguchi, H. Kasada and K. Ando, *Phys. Status Solidi B*, 2006, **243**, 950–954.
- 117 M. Y. Chen and C. C. Chang, *Jpn. J. Appl. Phys.*, 2009, **48**, 112201.
- 118 T. Abe, D. Katada, K. Miki, K. Tanaka, M. Nomura, Y. Inagaki, T. Tani, M. Ohtsuki, H. Kasada and K. Ando, *Phys. Status Solidi C*, 2010, **7**, 1706–1708.
- 119 P. Cheong, K. F. Chang, Y. H. Lai, S. K. Ho, I. K. Sou and K. W. Tam, *IEEE Trans. Ind. Electron.*, 2011, **58**, 5271–5277.
- 120 K. T. Lam, Y. J. Hsiao, L. W. Ji, T. H. Fang, K. H. Hsiao and T. T. Chu, *Nanoscale Res. Lett.*, 2017, **12**, 31.
- 121 Y. Li, Y. Song, Y. Jiang, M. Hu, Z. Pan, X. Xu, H. Chen, Y. Li, L. Hu and X. Fang, *Adv. Funct. Mater.*, 2017, **27**, 1701066.
- 122 Y. Liu, L. X. Pang, J. Liang, M. K. Cheng, J. J. Liang, J. S. Chen, Y. H. Lai and I. K. Sou, *IEEE Trans. Ind. Electron.*, 2018, **65**, 2737–2744.
- 123 S. V. Averin, P. I. Kuznetsov, V. A. Zhitov, L. Y. Zakharov and V. M. Kotov, *Opt. Quantum Electron.*, 2020, **52**, 1–7.
- 124 K. Benyahia, F. Djeflal, H. Ferhati, A. Bendjerad, A. Benhaya and A. Saidi, *J. Alloys Compd.*, 2021, **859**, 158242.
- 125 S. Yan, S. C. Rai, Z. Zheng, F. Alqarni, M. Bhatt, M. A. Retana and W. Zhou, *Adv. Electron. Mater.*, 2016, **2**, 1600242.
- 126 S. Sarkar, A. Das Mahapatra and D. Basak, *J. Colloid Interface Sci.*, 2018, **523**, 245–253.
- 127 R. Li, L. Tang, Q. Zhao, K. S. Teng and S. P. Lau, *Chem. Phys. Lett.*, 2020, **742**, 137127.
- 128 S. V. Averin, P. I. Kuznetsov, V. A. Zhitov, L. Y. Zakharov, V. M. Kotov, N. V. Alkeev and N. B. Gladisheva, *Semiconductors*, 2015, **49**, 1393–1399.
- 129 S. V. Averin, P. I. Kuznetsov, V. A. Zhitov, L. Y. Zakharov, V. M. Kotov and N. V. Alkeev, *Solid-State Electron.*, 2015, **114**, 135–140.